lubricants

MDPI

Article

Study of the Piston Secondary Movement on the Tribological Performance of a Single Cylinder Low-Displacement Diesel Engine

Jorge Duarte Forero [1,*], Guillermo Valencia Ochoa [1] and Wlamyr Palacios Alvarado [2]

[1] Programa de Ingeniería Mecánica, Universidad del Atlántico, Carrera 30 Número 8-49, Puerto Colombia, Barranquilla 080007, Colombia; guillermoevalencia@mail.uniatlantico.edu.co

[2] Facultad de Ingeniería, Universidad Francisco de Paula Santander, Avenida Gran Colombia No. 12E-96, Cúcuta 540003, Colombia; wlamyrpalacios@ufps.edu.co

* Correspondence: jorgeduarte@mail.uniatlantico.edu.co; Tel.: +575-3852266

Received: 22 September 2020; Accepted: 26 October 2020; Published: 30 October 2020

Abstract: The present study aims to analyze the secondary movement of the piston considering the deformations present in the piston skirt, the hydrodynamic lubrication, and the effects of the clearances in the connecting rod bearings. The analysis of the piston movement is performed by developing a mathematical model, which was used to evaluate the dynamic characteristics of the piston movement, the slap force on the piston skirt, the effect of the secondary piston movement on the connecting rod, and the influence of clearances in the connecting rod bearings and in the piston. For the study, the geometric of the crankshaft-connecting rod–piston system of a single-cylinder diesel engine is taken as a reference. The deformation model of the piston was carried out by means of a symmetric finite element model (FEM), which was integrated into the mathematical model of the piston. MATLAB® software (The MathWorks Inc., Natick, MA, USA) is used for the development of model simulations. The obtained results show that during the combustion cycle, there are six changes of direction in the secondary movement of the piston with lateral and angular velocities that can reach a magnitude of 0.13 m/s and 4 rad/s. The lateral and angular movement of the piston during its travel causes the appearance of impacts on the piston skirt with the cylinder liner, which produces an increase of approximately 500 N in the hydrodynamic forces in the connecting rod bearings. The force analysis shows that the range of the maximum magnitudes of these forces is between 1900 N and 3480 N. The increase in clearance between the cylinder liner and the piston skirt (Cpc) causes a greater lateral displacement and an increase in the angle of inclination of the piston. Analysis of the change in connecting rod bearing clearance shows that there are critical values in relation to clearance Cpc. The model presented allows us to analyze the different characteristics of the secondary movement of the piston, which involve the interaction between the piston skirt and the cylinder liner. Additionally, the influence of this movement on the connecting rod bearings is considered. The foregoing can be used as an analysis tool for the study of designs and/or modifications in the engine in such a way that greater durability of the components, reductions in acoustic emissions, and reduction in friction losses are achieved.

Keywords: clearances; deformation effects; diesel engine; piston secondary motion; tribological performance

1. Introduction

Inside the combustion chamber of the engines, there is a clearance between the cylinder liner and the piston skirt, which allows the piston to move in a lateral direction. Despite the presence of

the piston rings, this type of movement is not eliminated. The analysis of the lateral movement is of utmost importance since it allows us to understand the friction processes present in the piston, which constitute 30–50% of the total mechanical losses in engines [1]. Additionally, the clearance enables the piston to collide with the cylinder liner, generating unwanted vibrations and shocks in the cylinder block.

To transform the reciprocating movement of the combustion chamber into the rotational movement of the power shaft in internal combustion engines, the mechanism formed by the crankshaft, connecting rod, and piston is used [2–4]. Proper movement of this mechanism requires the presence of clearances, which are located at the connecting rod to the crankshaft connection, the connecting rod, and piston pin connection, and between the cylinder liner and the piston skirt. However, the presence of clearances and the contact forces between the cylinder liner and the piston cause lateral movements that cause the piston to tilt [5–8]. This particular movement is referred to in the literature as the secondary movement of the piston. The presence of this movement in the piston causes a negative effect on the engine due to the appearance of impacts and/or unbalanced hydrodynamic forces that can generate noise and vibrations in the engine body and in the connections of the crankshaft mechanism, connecting rod, and the piston [6,9,10]. Due to the above, the study of the clearances in the connecting rod connections with the piston and the crankshaft is an important condition that must be considered to analyze the dynamic behavior of the mechanism.

Several experimental investigations have focused on the study of the secondary movement of the piston [11–16]. The obtained results show that the piston impacts the cylinder liner an average of three times when completing a cycle of the combustion process. The strongest impact is located at the top dead center during the compression stroke [13,17,18]. Additionally, the results show that the piston tends to tilt during the expansion stage [14,19]. Each of the conditions described above is affected by clearances between the cylinder liner and piston and between the end connections of the connecting rod.

Additionally, research has been conducted focused on theoretical models to describe the secondary movement of the piston [20–23]. In these types of studies, the eccentricities of the piston with the cylinder liner are generally analyzed using moment and force equations. The presence of these moments and forces is a consequence of the pressure inside the combustion chamber, the inertia of the elements of the mechanism, the friction on the cylinder walls, and the impacts on the piston. The use of these theoretical models allows predicting the dynamic behavior of the piston. Tan and Ripin [22] developed a nonlinear model to describe the lateral and rotational motion of the piston. The research analyzed the secondary movement of the piston and its effect on engine vibration, which were validated by experimental results. Additionally, Tan and Ripin [24] studied the contact that occurs between the cylinder liner and the piston skirt due to the inclination and secondary movement of the piston. Murakami et al. [14] investigated an analysis methodology for secondary piston motion by adding structural analysis and multibody dynamic analysis. The proposed methodology was compared with results obtained by measuring the secondary movement, the tension in the piston skirt, and the vibration. In addition, later investigations involved the effects of surface roughness and lubrication conditions.

Meng et al. [25] analyzed the effects of vibration on tribological performance and lateral piston movement. The obtained results indicate that the vibration produced in the combustion chamber can be reduced by increasing the damping, mass of the cylinder, and rigidity. Narayan [26] developed a model of secondary piston movement, in which the dynamic characteristics of the cylinder liner and piston skirt were analyzed. Obert et al. [27] investigated the influence of temperature and the amount of lubricating oil on the piston skirt and cylinder. Mazouzi et al. [28] studied a numerical model to describe the secondary motion of the piston. The objective of the model is to observe the effect of the design parameters of the piston on the contact characteristics between the cylinder liner and the piston skirt. Results show that clearance changes can reduce piston strokes and friction. Fang et al. [29] developed a model to describe the lubrication in the piston skirt and the movement of the piston-connecting rod–crankshaft system. The model used allowed for the analysis of the

tribological behavior of the piston. Meng et al. [30] studied the influence of inertial forces on the lubrication film, including pressure changes in the film, hydrodynamic forces, and lateral movement of the piston.

Due to the importance of secondary piston motion analysis, researchers continually seek to expand the complexity of theoretical models to improve their estimation. One of these improvements is to consider the inertia of the connecting rod. Zhang et al. [31] implemented a mathematical model to describe the connecting rod–piston–crankshaft system. The model used considers the secondary movement of the piston and the force of the connecting rod. The results indicate that the center of mass is a significant parameter for the design of the connecting rod. Meng et al. [32,33] studied the dynamic movement of the piston, friction losses, and the lubrication film, taking into account the inertia of the connecting rod. The results showed that the inertia of the connecting rod significantly affects the dynamics of the piston, especially under high-speed conditions. Zhu et al. [34] analyzed the stress distribution in the connecting rod body, considering the effects of the lubrication film.

Another key factor to consider when studying the secondary movement of the piston is the deformation it experiences. The research focused on piston skirt lubrication analysis shows that piston deformation is an important factor in analyzing the friction characteristics applied to the engine body. Pelosi and Ivantysynova [35] analyzed the influence of heat flow and thermal deformation on the contact of the cylinder and the piston skirt. Ning et al. [36] developed a lubrication model in the piston skirt, considering the deformations of the piston. Since the deformation of the piston affects the lubrication conditions, it is necessary to consider it for the analysis of the secondary movement of the piston. However, generally, the deformations experienced by the piston are ignored for the development of the dynamic model. Additionally, research in the literature indicates that connecting rod clearances influence the dynamic behavior of the piston [37–40]. Despite the above, the clearances in the connecting rod connections are not normally considered in the dynamics of the piston movement.

The objective of the present investigation is to develop a mathematical model for the analysis of secondary movement of the piston that allows including the existing deformation in the piston skirt and the influence of the clearances in the connecting rod bearings in order to increase the complexity of the model to improve its estimates. For the study, the geometric of the crankshaft-connecting rod–piston system of a single-cylinder diesel engine is taken as a reference. The deformation model of the piston was carried out by means of a symmetric finite element model (FEM), which was integrated into the mathematical model of the piston. MATLAB software is used for the development of model simulations. The developed model is used to analyze the movement of the piston, the slap force on the piston skirt, the effect of the secondary movement of the piston on the connecting rod, and the influence of clearances on the connecting rod bearings and between the cylinder liner and the piston skirt.

The purpose of the foregoing is to develop a methodology to analyze in detail the characteristics of the secondary movement of the piston, which can be used as a tool for the diagnosis of slap forces, noise, and vibrations in the combustion chamber. The development of this type of tool is useful for the design and/or modifications to the engine in such a way that it facilitates the search for power reductions due to friction in the chamber, greater durability of the components, and lower acoustic emissions.

2. Dynamic Piston Model

The movement of the piston within the cylinder chamber presents three degrees of freedom, translation along the cylinder axis, lateral movement due to the clearance between the piston skirt and the cylinder liner, and a rotational movement caused by the piston pin. The translational movement is normally referred to as the primary movement of the piston, which is directly related to the angular movement of the crankshaft (see Section 2.1). The rotational and lateral movement is called the secondary movement of the piston and causes the appearance of contact forces (see Section 2.3). To consider both effects on the dynamic behavior of the piston, a mathematical model is made for each type of movement.

2.1. Piston Primary Motion Model

Figure 1 shows the general forces acting on the connecting rod and piston. The parameters of the distances considered for the dynamic model are shown in Table 1.

Table 1. Reference distance for the dynamic model.

Parameter	Value
Distance (a)	24 mm
Length of piston skirt (L_{ps})	48 mm
Distance (b)	35 mm
Crankshaft radius (r)	48 mm
Length of connecting rod (L_{cr})	106 mm
Distance (l_1)	28 mm
Distance (l_2)	78 mm
Piston radius (r_p)	39 mm

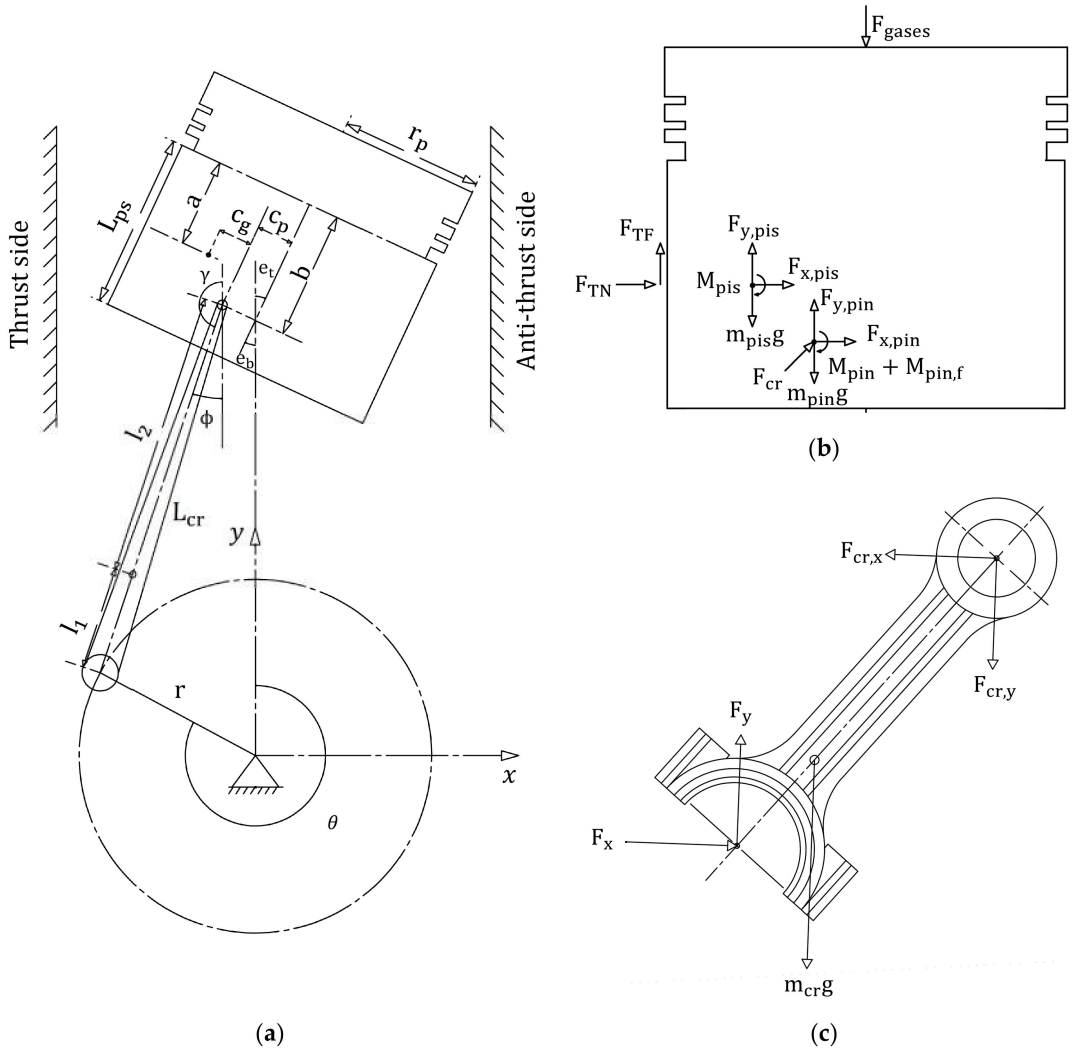

Figure 1. (**a**) Crankshaft-connecting rod–piston system, (**b**) forces on piston, and (**c**) forces on the connecting rod.

Considering the distribution of forces shown in Figure 1b, the following equilibrium conditions of forces and moments in the piston are established:

$$\sum F_x = F_{x,pis} + F_{x,pin} + F_{cr,x} + F_{TN} = 0 \tag{1}$$

$$\sum F_y = F_{y,pis} + F_{y,pin} + F_{cr,y} - m_{pis}g - m_{pin}g + F_{TF} - F_{gases} = 0 \tag{2}$$

$$\sum M = M_{pis} + M_{pin} + M_{pin,f} + F_{gases}{\cdot}c_p - m_{pis}g{\cdot}c_g + F_{x,pis}{\cdot}(b-a) + F_{y,pis}{\cdot}c_g = 0 \tag{3}$$

where $F_{x,pis}$, $F_{x,pin}$ and $F_{cr,x}$ are the inertial force of the piston, the inertial force of the pin piston, and the reaction force of the connecting rod in the pin piston in the lateral direction, respectively. Similarly, $F_{y,pis}$, $F_{y,pin}$ and $F_{cr,y}$ indicate each of the above forces acting in the transverse direction, respectively. F_{TN}, F_{TF} and F_{gases} represent the lateral force acting on the piston skirt, the total frictional force on the piston skirt, and the force of the combustion gases acting on the top of the piston. M_{pis}, M_{pin} and $M_{pin,f}$ are the moment of inertia of the piston, the total moment about the pin piston due to normal forces, and the total moment about pin piston due to friction forces. m_{pis} and m_{pin} represent the mass of the piston and the mass of the pin piston.

The inertial forces acting on the piston are defined by the following equations:

$$F_{x,pis} = -m_{pis}{\cdot}\left[\frac{a\left(\ddot{e}_b - \ddot{e}_t\right)}{L_{ps}} + \ddot{e}_t\right] \tag{4}$$

$$F_{x,pin} = -m_{pin}{\cdot}\left[\frac{b\left(\ddot{e}_b - \ddot{e}_t\right)}{L_{ps}} + \ddot{e}_t\right] \tag{5}$$

$$F_{y,pis} = m_{pis}{\cdot}r\dot{\theta}^2\left[\sin\theta\tan\phi + \cos\theta{\cdot}\left(1 + \frac{r\cos\theta}{L_{cr}\cos\phi}{\cdot}\left(1+\tan^2\phi\right)\right)\right] \tag{6}$$

$$F_{y,pin} = m_{pin}{\cdot}r\dot{\theta}^2\left[\sin\theta\tan\phi + \cos\theta{\cdot}\left(1 + \frac{r\cos\theta}{L_{cr}\cos\phi}{\cdot}\left(1+\tan^2\phi\right)\right)\right] \tag{7}$$

where θ and ϕ are the angles that describe the rotational motion of the crankshaft and connecting rod. e_t and e_b are the eccentricities of the piston at the top and bottom. r and L_{cr} are the radius of the crankshaft and the length of the connecting rod.

Taking into account the forces acting on the connecting rod (see Figure 1c), the equilibrium equations are defined:

$$\sum F_x = F_{cr,x} - vv - m_{cr}\ddot{X}_{cr} = 0 \tag{8}$$

$$\sum \vec{F}_y = F_{cr,y} - F_y - m_{cr}\ddot{Y}_{cr} - m_{cr}g = 0 \tag{9}$$

$$F_y l_1 \sin\phi - F_x l_1 \cos\phi + F_{cr,y} l_2 \sin\phi - F_{cr,x} l_2 \cos\phi = \ddot{\phi} I_{cr} \tag{10}$$

where I_{cr} is the rotational moment of inertia of the connecting rod with respect to the center of mass. $\ddot{X}_{cr}$ and $\ddot{Y}_{cr}$ are the horizontal and vertical accelerations of the center of mass of the connecting rod, which are defined by the following equations.

$$\ddot{X}_r = \left(\frac{l_1}{L_{cr}}\right)\frac{b}{L_{ps}}\ddot{e}_b + \frac{l_1}{L_{cr}}\left(1 - \frac{b}{L_{ps}}\right)\ddot{e}_t - \dot{\theta}^2 r\left(1 - \frac{l_1}{L_{cr}}\right)\sin\theta \tag{11}$$

$$\ddot{Y}_r = -r\dot{\theta}^2\left[\frac{l_1}{L_{cr}}\sin\theta\tan\phi + \cos\theta{\cdot}\left(1 + \frac{l_1}{L_{cr}}{\cdot}\frac{r\cos\theta}{L_{cr}\cos\phi}{\cdot}\left(1+\tan^2\phi\right)\right)\right] \tag{12}$$

where L_{ps} is the length of the piston skirt.

From the previous equations, the dynamic movement of the piston can be described, as shown below:

$$\begin{bmatrix} \vec{F}' - F_{TF}\tan\phi + F_{TN} \\ M_{pis} + M_{pin} + M_{pin,f} \end{bmatrix} = \begin{bmatrix} m_{pin}\left(1-\frac{b}{L_{ps}}\right) + m_{pis}\left(1-\frac{a}{L}\right) + \left(\frac{l_1}{L_{cr}}\right)^2 m_{cr}\left(1-\frac{b}{L_{ps}}\right) & m_{pin}\frac{b}{L_{ps}} + m_{pis}\frac{a}{L} + \left(\frac{l_1}{L_{cr}}\right)^2 m_{cr}\frac{b}{L_{ps}} \\ m_{pis}\left(1-\frac{a}{L_{ps}}\right)(b-a) + \frac{I_{pis}}{L_{ps}} & m_{pis}\frac{a}{L}(b-a) - \frac{I_{pis}}{L_{ps}} \end{bmatrix} \times \begin{bmatrix} \ddot{e}_t \\ \ddot{e}_b \end{bmatrix} \quad (13)$$

where I_{pis} is the rotational moment of inertia of the piston with respect to the center of mass. The force $F\prime$ is defined as:

$$F' = \tan\phi\left[F_{gases} + \ddot{Y}_p m_p + m_p g + \frac{l_1}{L_{cr}}\left(\ddot{Y}_{cr} m_{cr} + m_{cr} g\right)\right] + \frac{l_1}{L_{cr}} m_{cr}\dot{\theta}^2 r(1-\frac{l_1}{L_{cr}})\sin\theta - \frac{\ddot{\phi} I_{cr}}{L_{cr}\cos\phi} \quad (14)$$

$\ddot{\phi}$ is defined by the following equation:

$$\ddot{\phi} = \dot{\theta}^2\left[\tan\phi\left(\frac{r\cos\theta}{L_{cr}\cos\phi}\right)^2 + \frac{r\sin\theta}{L_{cr}\cos\phi}\right] \quad (15)$$

2.2. Hydrodynamic Lubrication Model

The total normal force (F_{TN}) acting on both sides of the piston, the total friction force (F_{TF}) acting on the surface of the piston skirt, the total moment applied on the pin piston due to normal forces $\left(M_{pin}\right)$ and the total moment on the pin piston due to friction forces $\left(M_{pin,f}\right)$ are the consequence of the combined effect of hydrodynamic forces and solid–solid contact forces. Therefore, each of the above forces and moments can be expressed as follows:

$$F_{TN} = F_{TN,h} + F_{TN,c} \quad (16)$$

$$F_{TF} = F_{TF,h} + F_{TF,c} \quad (17)$$

$$M_{pin} = M_{pin,h} + M_{pin,c} \quad (18)$$

$$M_{pin,f} = M_{pin,fh} + M_{pin,fc} \quad (19)$$

where $F_{TN,h}$, $F_{TF,h}$, $M_{pin,h}$ and $M_{pin,fh}$ are a consequence of the hydrodynamic film and $F_{TN,c}$, $F_{TF,c}$, $M_{pin,c}$ and $M_{pin,fc}$ are produced by the solid–solid contact.

Since force and moment do not have linear behavior, the pressure of the lubrication film is not evenly distributed. Due to the above, the Reynolds hydrodynamic lubrication model is considered [41,42], established as:

$$\frac{\partial}{\partial x}\left(\phi_x h^3 \frac{\partial p}{\partial x}\right) + \frac{\partial}{\partial y}\left(\phi_y h^3 \frac{\partial p}{\partial y}\right) = 6\mu U\left(\frac{\partial h}{\partial y} + \sigma\frac{\partial \phi_s}{\partial y}\right) + 12\mu\frac{\partial h}{\partial t} \quad (20)$$

where x and y are the coordinate axes described in Figure 1, φ_x and φ_y are the pressure flow factors, μ is the dynamic viscosity of the lubrication film, φ_s is the shear flow factor, p is the pressure of the film, U is the piston velocity, and σ is the surface roughness.

The thickness of the lubrication film (h) is described by the following equation:

$$h = c_{pc} + e_t\cos\theta + \frac{y}{L_{ps}}\cos\theta\cdot(e_b - e_t) + d \quad (21)$$

where c_{pc} is the clearance between the piston skirt and the cylinder liner, and d is the elastic deformation of the piston caused by the pressure of the lubrication film. Details for the calculation of the piston deformation functions are shown in Section 2.5.

The hydrodynamic pressure of the film produces the normal hydrodynamic force $\left(F_{TN,h}\right)$ applied at the piston skirt and the moment at the piston pin $\left(M_{pin,h}\right)$, which are calculated using the following equations:

$$F_{TN,h} = \int_0^{L_{ps}} \int_0^{2\pi} r_p \cdot p \cdot \cos\varphi d\varphi dy \tag{22}$$

$$M_{pin,h} = \int_0^{L_{ps}} \int_0^{2\pi} r_p \cdot p \cdot (b-y) \cos\varphi d\varphi dy \tag{23}$$

where r_p is the radius of the piston.

The shear stress in the piston skirt is determined by the following expression:

$$\tau = \frac{-\left(\Psi_f + \Psi_{fs}\right)\mu U}{h} + \Psi_{fp}\frac{h}{2}\frac{\partial p}{\partial y} \tag{24}$$

where Ψ_f, Ψ_{fs} and Ψ_{fp} are shear stress factors used to consider the effects of surface roughness and waviness.

From the shear stress, the friction force $\left(F_{TF,h}\right)$ and moment on the pin piston $\left(M_{pin,fh}\right)$ due to hydrodynamic friction are calculated using the following equations:

$$F_{TF,h} = \int_0^{L_{ps}} \int_0^{2\pi} r_p \cdot \tau d\varphi dy \tag{25}$$

$$M_{pin,fh} = \int_0^{L_{ps}} \int_0^{2\pi} r_p \cdot \tau \cdot \left(r_p \cos\varphi - c_p\right) d\varphi dy \tag{26}$$

The contact pressure distribution is calculated using the Greenwood and Tripp rough contact model [43], as shown below:

$$p_w = \frac{16\sqrt{2}}{15} \cdot \left(\pi\eta\frac{\sigma^{\frac{3}{2}}}{\beta^{\frac{1}{2}}}\right) \cdot E' \cdot F_{\frac{5}{2}} \tag{27}$$

where E' is the compound elastic modulus, η is the asperity density, β is the curvature radius of the convex peak, and $F_{\frac{5}{2}}$ is the commutation function define as follows:

$$F_{\frac{5}{2}} = \begin{cases} 4.41 \times 10^{-5}(4 - H_s)^{6.81}, & when\ H_s < 4 \\ 0, & when\ H_s \geq 4 \end{cases} \tag{28}$$

where H_s is the film thickness ratio.

The compound elastic modulus (E') is determined by the following expression:

$$E' = \frac{2}{\frac{1-\nu_1{}^2}{E_1} + \frac{1-\nu_2{}^2}{E_2}} \tag{29}$$

where ν_1 and ν_2 are the Poisson's ratio of the piston and the cylinder liner, and E_1 and E_2 are Young's modulus of the piston and the cylinder liner, respectively.

From the distribution of the contact pressure (p_w) it is possible to determine the forces and moments associated with the solid–solid contact. Each of these calculations are performed using the following expressions:

$$F_{TN,c} = \int_0^{L_{ps}} \int_0^{2\pi} r_p \cdot p_w \cdot \cos\varphi d\varphi dy \tag{30}$$

$$F_{TF,c} = \int_0^{L_{ps}} \int_0^{2\pi} r_p \cdot p_w \cdot \mu_f d\varphi dy \tag{31}$$

$$M_{pin,c} = \int_0^{L_{ps}} \int_0^{2\pi} r_p \cdot p_w \cdot (b - y) \cos\varphi d\varphi dy \tag{32}$$

$$M_{pin,fc} = \int_0^{L_{ps}} \int_0^{2\pi} r_p \cdot p_w \cdot \mu_f \cdot \left(r_p \cos\varphi - c_p\right) d\varphi dy \tag{33}$$

where μ_f is the coefficient of contact friction.

2.3. Piston Secondary Motion Model

The interaction between the cylinder liner and the piston skirt is modeled with two degrees of freedom, as shown in Figure 2. The piston is separated from the cylinder liner by a clearance, which allows the piston to perform a lateral movement and a rotary movement on the pin piston. During engine operation, the secondary movement of the piston causes the presence of contact forces at the four corners of the piston [43]. These contact points are identified by the numbers 1, 2, 3 and 4. The contact forces are represented as F_1, F_2, F_3 and F_4, respectively. The contacts between the cylinder liner and the piston skirt are modeled as a damping system consisting of rigidity constants (k_s, k_{cs}) and damping constants (c_d, c_{cd}). Figure 3 shows the geometric parameters of angles and distances in the piston used to describe the contact forces.

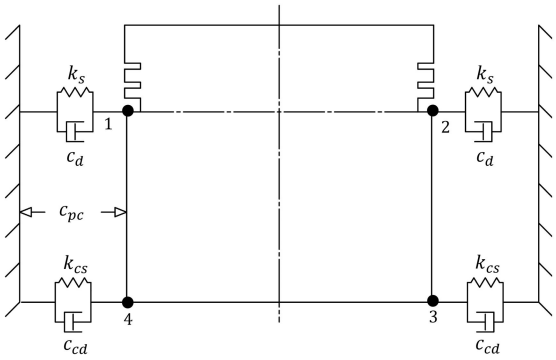

Figure 2. Piston secondary motion model.

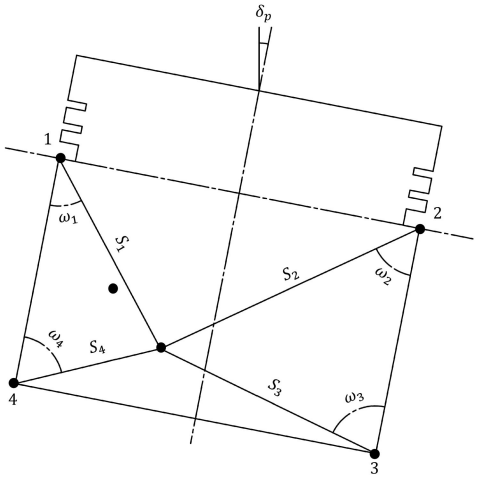

Figure 3. Geometric parameters of the piston model.

The displacements of the piston center of mass and the center of mass of the piston pin are determined by the following equations.

$$x_{pis} = x_{pin} + \sqrt{(b-a)^2 + {c_g}^2} \cdot \sin\left(\tan^{-1}\left[\frac{c_g}{b-a}\right] - \delta_p\right) \tag{34}$$

$$y_{pis} = y_{pin} + \sqrt{(b-a)^2 + {c_g}^2} \cdot \cos\left(\tan^{-1}\left[\frac{c_g}{b-a}\right] - \delta_p\right) \tag{35}$$

Applying the second derivative in Equations (16) and (17), the accelerations of the center of mass of the piston and the center of mass of the piston pin are obtained.

$$\ddot{x}_{pis} = \ddot{x}_{pin} - \sqrt{(b-a)^2 + {c_g}^2} \cdot \sin\left(\tan^{-1}\left[\tfrac{c_g}{b-a}\right] - \delta_p\right)\dot{\delta}_p{}^2 - \sqrt{(b-a)^2 + {c_g}^2} \cdot \cos\left(\tan^{-1}\left[\tfrac{c_g}{b-a}\right] - \delta_p\right)\ddot{\delta}_p \tag{36}$$

$$\ddot{y}_{pis} = \ddot{y}_{pin} - \sqrt{(b-a)^2 + {c_g}^2} \cdot \cos\left(\tan^{-1}\left[\tfrac{c_g}{b-a}\right] - \delta_p\right)\dot{\delta}_p{}^2 + \sqrt{(b-a)^2 + {c_g}^2} \cdot \sin\left(\tan^{-1}\left[\tfrac{c_g}{b-a}\right] - \delta_p\right)\ddot{\delta}_p \tag{37}$$

The displacement of the contact points 1, 2, 3, and 4 are determined by the following equations:

$$x_1 = s_1 \sin\left(\omega_1 + \delta_p\right) - s_1 \sin\omega_1 - x_{ps} \tag{38}$$

$$x_2 = s_2 \sin\left(\omega_2 - \delta_p\right) - s_2 \sin\omega_2 + x_{ps} \tag{39}$$

$$x_3 = s_3 \sin\left(\omega_3 + \delta_p\right) - s_3 \sin\omega_3 + x_{ps} \tag{40}$$

$$x_4 = s_4 \sin\left(\omega_4 - \delta_p\right) - s_4 \sin\omega_4 - x_{ps} \tag{41}$$

Through the first derivative of Equations (38)–(41), the following relationships are obtained:

$$\dot{x}_1 = s_1\dot{\delta}_p \cos\left(\omega_1 + \delta_p\right) - \dot{x}_{ps} \tag{42}$$

$$\dot{x}_2 = -s_2\dot{\delta}_p \cos\left(\omega_2 - \delta_p\right) + \dot{x}_{ps} \tag{43}$$

$$\dot{x}_3 = s_3\dot{\delta}_p \cos\left(\omega_3 + \delta_p\right) + \dot{x}_{ps} \tag{44}$$

$$\dot{x}_4 = -s_4\dot{\delta}_p \cos\left(\omega_4 - \delta_p\right) - \dot{x}_{ps} \tag{45}$$

From the previous equations, the contact forces can be defined, as shown below:

$$F_1 = k_s\left(x_1 - c_{pc}\right) + c_d\dot{x}_1 \tag{46}$$

$$F_2 = k_s\left(x_2 - c_{pc}\right) + c_d\dot{x}_2 \tag{47}$$

$$F_3 = k_{cs}\left(x_3 - c_{pc}\right) + c_{cd}\dot{x}_3 \tag{48}$$

$$F_4 = k_{cs}\left(x_4 - c_{pc}\right) + c_{cd}\dot{x}_4 \tag{49}$$

2.4. Connecting Rod Clearance Model

This section describes the forces acting on the connecting rod bearings. Figure 4 shows the geometric parameters and the forces in the cross-section of the connecting rod bearings.

To determine the forces in the big and small bearing of the connecting rod, the isothermal Reynolds equation [44] is used.

$$6U_r\frac{\partial h}{\partial x} + 12\frac{\partial h}{dt} = \frac{\partial}{\partial x}\left(\frac{h^3}{\mu}\frac{\partial p_r}{\partial x}\right) + \frac{\partial}{\partial z}\left(\frac{h^3}{\mu}\frac{\partial p_r}{\partial z}\right) \tag{50}$$

where x and z represent the radial direction and axial direction, U_r is the relative tangential velocity between the journal and bearing surfaces and p_r is the pressure of the lubrication film between the journal and the bearing. Due to the complexity of the Reynolds equation, the infinitely short journal

bearing approach proposed by DuBois and Ocvirk [45] was implemented. In this way, the Reynolds equation can be rewritten as follows:

$$6U_r\frac{\partial h}{\partial x}+12\frac{\partial h}{dt}=\frac{\partial}{\partial z}\left(\frac{h^3}{\mu}\frac{\partial p_r}{\partial z}\right) \tag{51}$$

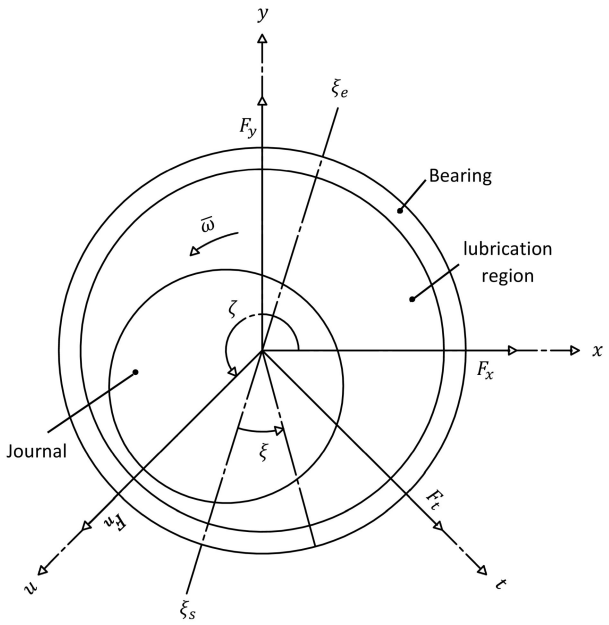

Figure 4. Bearing cross-section.

The pressure of the lubrication film is established by means of Equation (36) [36].

$$p_r=\frac{3\mu c_{rc}\left(4z^2-{L_{jb}}^2\right)}{2h^3}\cdot\left(\dot{e}_r\cos\xi+e_r\left[\dot{\zeta}-\overline{\omega}\right]\cdot\sin\xi\right) \tag{52}$$

where L_{jb} is the length of the journal–bearing, $\overline{\omega}$ is the average angular velocity between the bearing and the journal and c_{rc} is the radial clearance. The thickness of the lubrication film (h) is calculated through the following equation:

$$h=c_{rc}(1-e_r\cos\xi) \tag{53}$$

e_r represents the eccentricity ratio between the journal and the bearing. The calculation of e_r is carried out using the following equation:

$$e_r=\frac{\sqrt{\left(x_b-x_{pin}\right)^2+\left(y_b-y_{pin}\right)^2}}{c_{jb}} \tag{54}$$

$$\dot{e}_r=\frac{\left(y_b-y_{pin}\right)\left(\dot{y}_b-\dot{y}_{pin}\right)+\left(x_b-x_{pin}\right)\left(\dot{x}_b-\dot{x}_{pin}\right)}{c_{jb}\cdot e_d} \tag{55}$$

where c_{jb} and e_d are the radial clearance between the journal–bearing and eccentricity distance. x_b and y_b are the displacement of the bearing in the horizontal and vertical direction.

The angle $\dot{\zeta}$ in Equation (56) is determined from the following equation:

$$\dot{\zeta}=\frac{\left(\dot{y}_b-\dot{y}_{pin}\right)\left(x_b-x_{pin}\right)-\left(y_b-y_{pin}\right)\left(\dot{x}_b-\dot{x}_{pin}\right)}{{e_d}^2} \tag{56}$$

The displacement (x_b, y_b) and velocities $\left(\dot{x}_b, \dot{y}_b\right)$ of the bearing are calculated using the following equations:

$$x_b = x_{cr} + l_1 \sin\gamma \tag{57}$$

$$y_b = y_{cr} - l_1 \cos\gamma \tag{58}$$

$$\dot{x}_b = \dot{x}_{cr} + \dot{\gamma} l_1 \cos\gamma \tag{59}$$

$$\dot{y}_b = \dot{x}_{cr} + \dot{\gamma} l_1 \sin\gamma \tag{60}$$

The tangential and normal hydrodynamic force on the bearing is determined by integrating the lubrication film around the bearing, as shown in the following equations:

$$F_t = \int_0^{L_{jb}} \int_{\xi_s}^{\xi_e} r{\cdot}p_r{\cdot}\sin\xi d\xi dz \tag{61}$$

$$F_n = \int_0^{L_{jb}} \int_{\xi_s}^{\xi_e} r{\cdot}p_r{\cdot}\cos\xi d\xi dz \tag{62}$$

where ξ_s and ξ_e are the start and the end angle.

Hydrodynamic forces (F_t and F_n) along the x and y axes can be defined as follows:

$$F_{b,x} = F_n \cos\zeta - F_t \sin\zeta = F_{cr,x} \tag{63}$$

$$F_{b,y} = F_n \sin\zeta + F_t \cos\zeta = F_{cr,y} \tag{64}$$

2.5. Deformation Model

Equation (21) shown in Section 2.2 describes the thickness of the lubrication film, which is influenced by the functions of the deformation of the piston. Since the piston is deformed by the pressure of the lubrication film along with the skirt of the piston, elastic deformation occurs, which influences the clearance and, therefore, the slap forces on the piston. Due to this, the dynamic study of the piston must consider this deformation.

The elastic deformation of the piston is due to the combination of hydrodynamic pressure and contact pressure. To describe this deformation, a compliance matrix is used that is generated by a symmetric finite element model (FEM). The generation of the piston compliance matrix is shown in Figure 5.

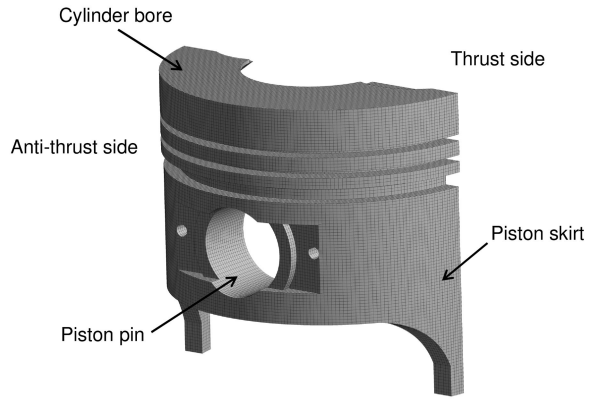

Figure 5. Generation of compliance matrix.

The matrix shown in Figure 5 is used to calculate the elastic deformation of the piston in the radial direction caused by the contact forces and the hydraulic pressure of the lubrication film. For the construction of the matrix, a hexahedral type mesh is used, formed by 376,000 nodes and

350,000 elements. The characteristics of the meshing are in agreement with those reported in the literature [46,47].

Equation (65) is used to determine the elastic deformation in the piston skirt.

$$d = \left[C_{ij}^{\theta y}\right] \cdot (p_w + p) \tag{65}$$

where $C_{ij}^{\theta y}$ is the elastic compliance matrix, which indicates the displacement of each node (i, j); p is the hydrodynamic pressure; and p_w is the contact pressure. Each of these pressures is determined by Equations (20) and (27). To verify the appropriate number of mesh elements, a mesh independence analysis is performed, in which the deformation obtained at different points along the piston skirt is compared (see Figure 6). The results of the independence analysis are shown in Figure 7.

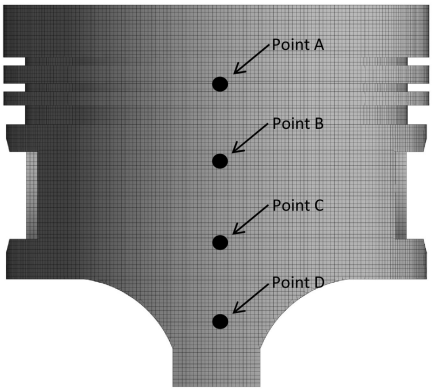

Figure 6. Reference points for mesh independence analysis.

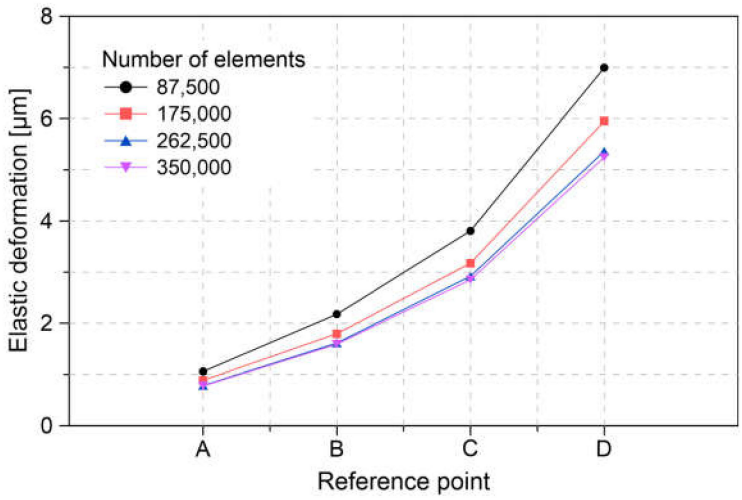

Figure 7. Elastic deformation of the piston skirt for different meshes.

The results of Figure 7 show that from a number of elements of 350,000, the difference between the deformation estimates is less than 3%. Due to this small difference, 350,000 elements are selected to build a suitable mesh without causing high computation times.

2.6. Numerical Methodology

To solve the equations described in the dynamic model of the piston, the solver ode45 of the MATLAB software is used. Figure 8 shows the process diagram used to study the dynamics of the piston.

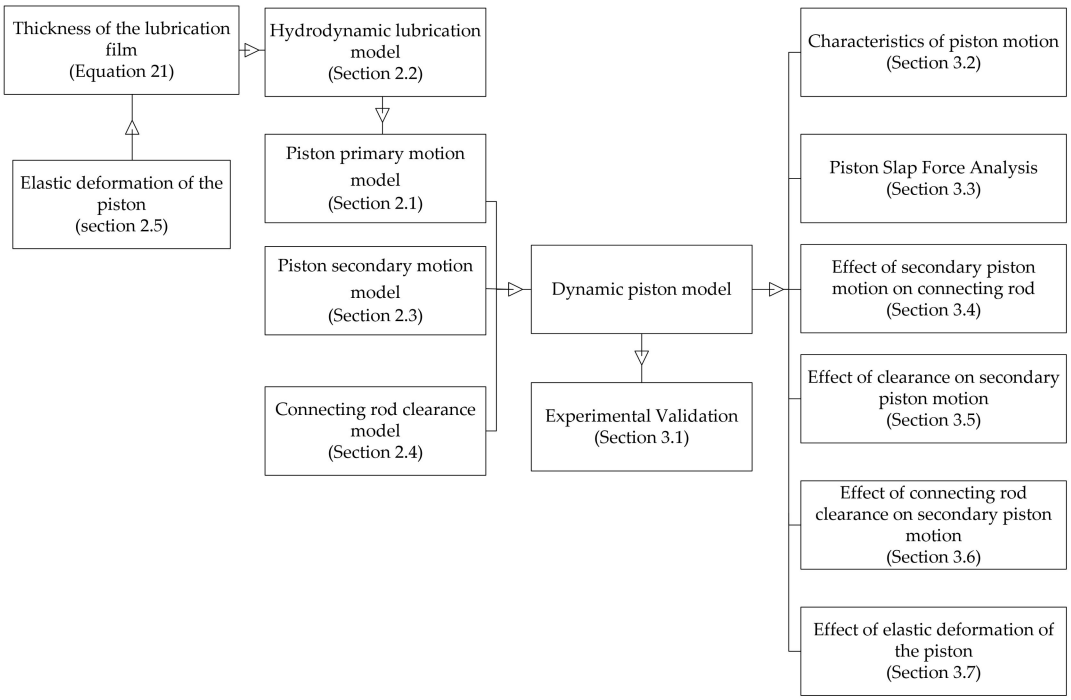

Figure 8. Methodology for the dynamic analysis of the piston.

The dynamic model of the piston is made up of three sub-models, which are used to describe the primary and secondary movement of the piston and the behavior of the clearances in the connecting rod bearings. The model is complemented with the deformation data of the piston skirt, which are calculated using a finite element model (FEM). This deformation makes it possible to improve the estimation of the thickness of the lubrication film, which is used in the hydrodynamic model of the piston.

The response of the dynamic piston model is validated by a comparison with experimental data obtained through the development of tests on a test bench. Finally, the model estimates are used to study the characteristics of movement and forces in the piston.

3. Results and Discussion

3.1. Experimental Validation

To determine the validity of the mathematical model used in the present study, a comparison is made between the results obtained by means of the model and those obtained by means of experimental tests. The experimental test bench used is shown in Figure 9.

The combustion pressure curve for this operating condition is shown in Figure 10. The experimental data are recorded with a pitch length corresponding to 2 degrees of the crank angle. The data from the sensors located on the piston are connected to a data acquisition system and post-processing software. During engine operation, variations from cycle to cycle may occur as a result of changes in combustion chamber pressure. Additionally, the irregularity of the lubrication system due to the splash mechanism in the cylinder liner causes variations in the lubrication film that affect the damping between the piston skirt and the cylinder liner. As a result, the data are recorded for 30 cycles of the engine in order to minimize errors due to the repeatability of the measurements.

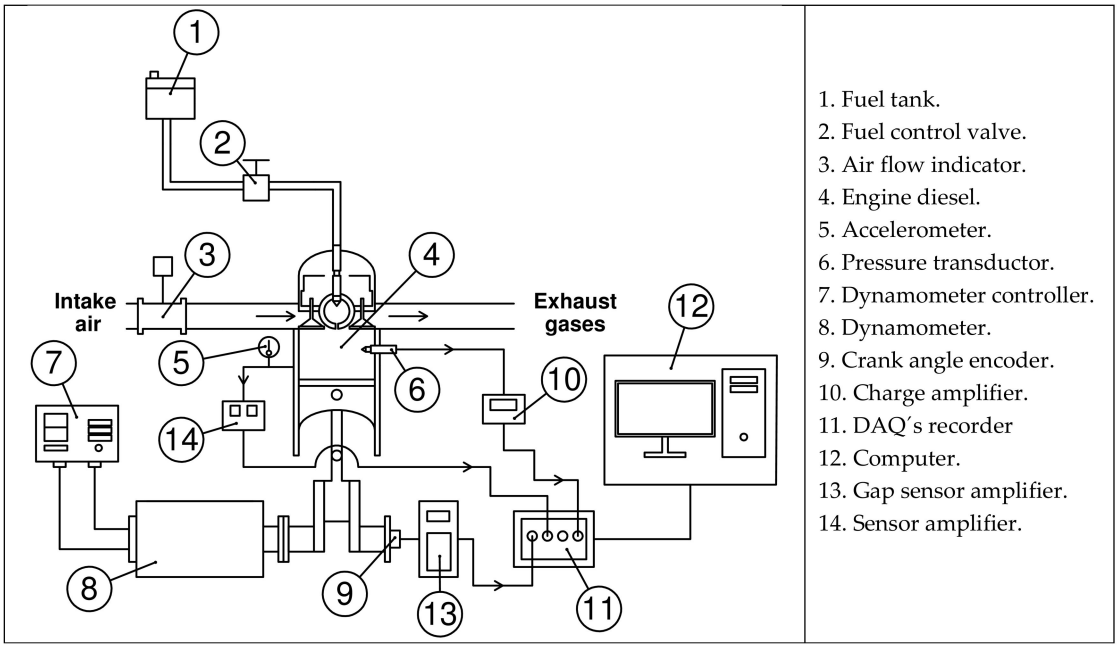

Figure 9. Experimental test bench.

The measurement of the crankshaft rotational speed was carried out by means of an angle sensor (Beck Arnley 180-0420, Nashville, TN, USA). Using a piezoelectric sensor (KISTLER type 7063-A, Winterthur, Switzerland) installed inside the combustion chamber, the combustion pressure is recorded.

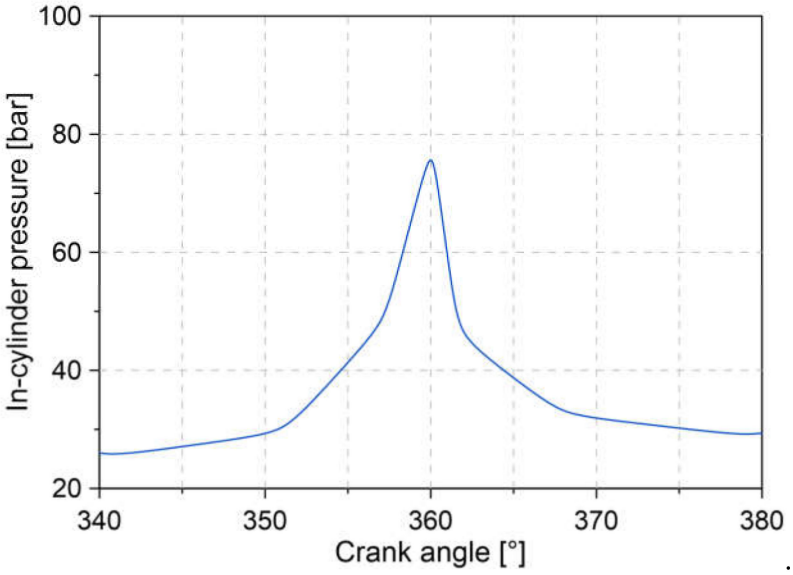

Figure 10. Engine pressure curve (3600 rpm, 9 Nm).

The technical characteristics of the engine used are shown in Table 2. Four eddy current sensors located on the edges of the piston skirt are used to monitor the piston slap behavior (see Figure 11). The sensors are embedded in the piston and are connected through a link system that runs through the connecting rod–crankshaft system until it reaches a signal amplifier. By means of the alternator connected to the engine, rotation speed and a constant load of 3600 rpm and 9 Nm are established due to these are the main operating conditions. This is due to the fact that in this condition of torque and rotational speed, maximum efficiency is produced in the stationary diesel engine.

Table 2. Stationary diesel engine.

Model	SK-MDF300
Manufacturer	SOKAN
Engine type	1 cylinder
Bore x stroke	78 mm × 62.57 mm
Cycle	4 Strokes
Maximum power	4.6 hp at 3600 rpm
Compression ratio	20:1
Injection system	Direct injection
Displaced volume	299 CC
Intake system	Naturally Aspirated

Table 3 shows the instruments used to measure the magnitudes of pressure in the cylinder chamber and the crankshaft angle. To measure the clearance between the piston skirt and the cylinder liner, a non-contact gap sensor (Model HPC-500-V, Ayer, MA, USA) was selected, with high thermal resistance (800 °C) and a resolution of 0.25 µm.

Table 3. Measuring instruments.

Parameter	Instrument	Manufacturer	Range	Uncertainty (%)
Cylinder pressure	Piezoelectric transducer	KISTLER	0–250 bar	±0.5
Angle	Crankshaft angle	Beck Arnley	5–9999 RPM	±1.0
Clearance	Gap sensor	Capacitec	0–2.5 mm	±0.2

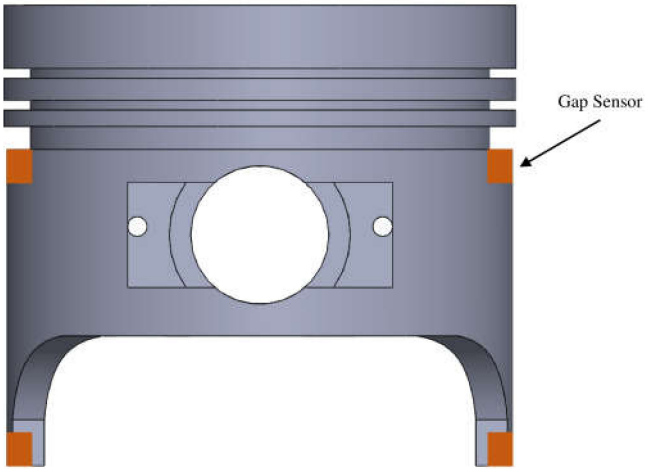

Figure 11. Piston gap sensors.

Figure 12 shows the comparison between the clearances between the piston skirt and the cylinder liner obtained through the simulation of the model and the experimental results.

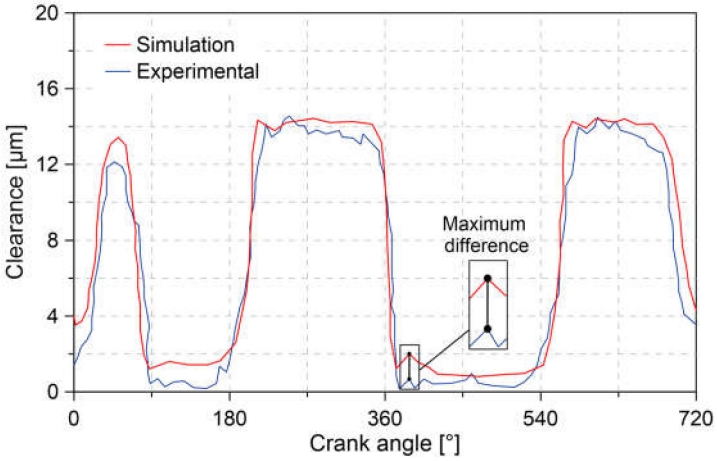

(**a**)

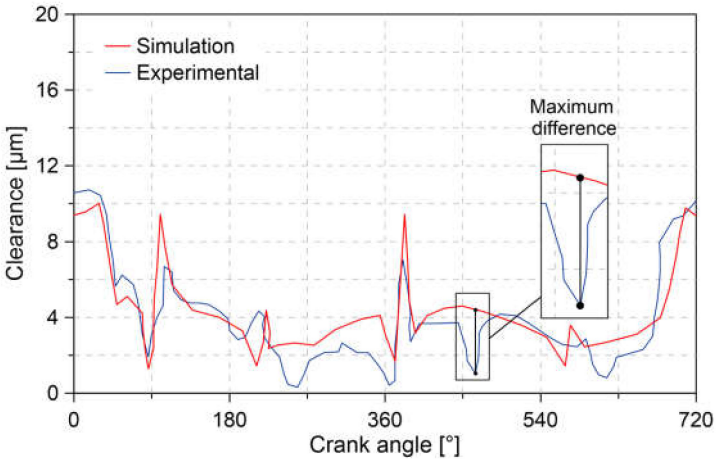

(**b**)

Figure 12. Comparison of clearance between model and experimental data: (**a**) upper thrust side and (**b**) lower thrust side.

The obtained results show that both curves maintain the same trends both in the upper part and in the lower part of the piston. In the case of measurements of clearances at the top of the piston, an average error of 14% was observed between the model estimates and the experimental data (see Figure 12a). However, there are regions throughout the combustion cycle in which a greater distance is observed. This may be the result of the sum of factors such as sudden pressure variations in the chamber, changes in the thickness of the lubrication film, and alteration in the properties of the lubricant.

For the measurements of the clearances at the lower of the piston, an average error of 18% was observed between the model estimates and the experimental data. In a similar way to the previous case, regions of separation were observed in which a greater difference between the model and the experimental one can be seen. However, for the lower of the piston, the separation regions are larger when compared to the results in Figure 12a. This greater separation can be attributed to surface irregularities present in the lower part of the cylinder liner.

In general, the trend of the model estimates and the experimental data, and the percentage of error, are similar to those reported in the literature [13].

3.2. Characteristics of Piston Motion

In Figures 13 and 14, the characteristics of the secondary motion of the piston during a combustion cycle are described.

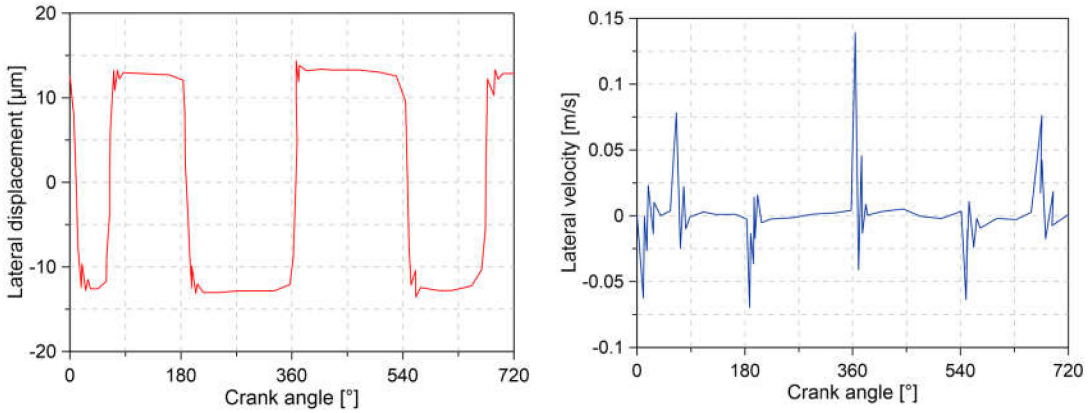

Figure 13. (**a**) Lateral motion and (**b**) lateral velocity of the piston.

Figure 13 shows the lateral displacement experienced by the piston and the velocity of this displacement. The positive and negative displacements shown in Figure 13a demonstrate that the piston performs a fluctuating motion in the lateral direction while completing the stroke of a combustion cycle. This can cause the appearance of impacts of the piston skirt with the cylinder liner. The maximum lateral displacement of the piston is 14 µm.

The velocity of the lateral motion is shown in Figure 13b. It was observed that the velocity peaks are located in the vicinity of the crankshaft angles 0°, 180°, 360°, 540°, and 720°, which correspond to the location of the top and bottom dead centers of the piston. This behavior is in agreement with the research presented in the literature [13,48]. Lateral velocity analysis shows that six changes in the direction of secondary piston movement occur during the combustion cycle. The maximum lateral velocity is 0.13 m/s, which is located between an angle of 357° and 370°.

The piston tilting angle is shown in Figure 14. The results show that the piston performs a rotary movement in a range of -3.4×10^{-4} to 2.2×10^{-4} rad. The maximum angular velocity reached was 3.75 rad/s, obtained in the final stage of the compression process.

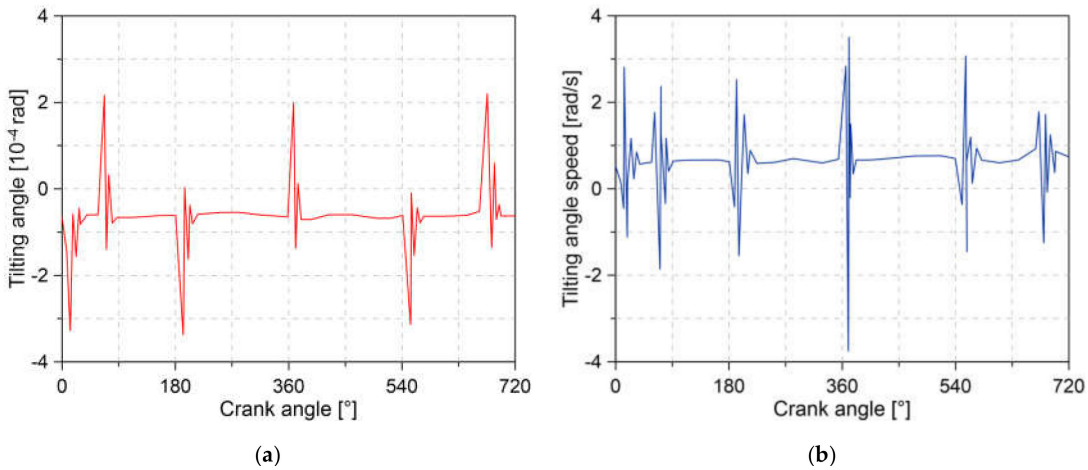

Figure 14. (**a**) Tilting angle and (**b**) tilting angle speed of the piston.

The fluctuating motion in the lateral direction of the piston described in Figure 13a can be related to the forces present in the connecting rod bearing $(F_{cr,x})$. Figure 15 describes the values taken by the force $(F_{cr,x})$ throughout the combustion cycle.

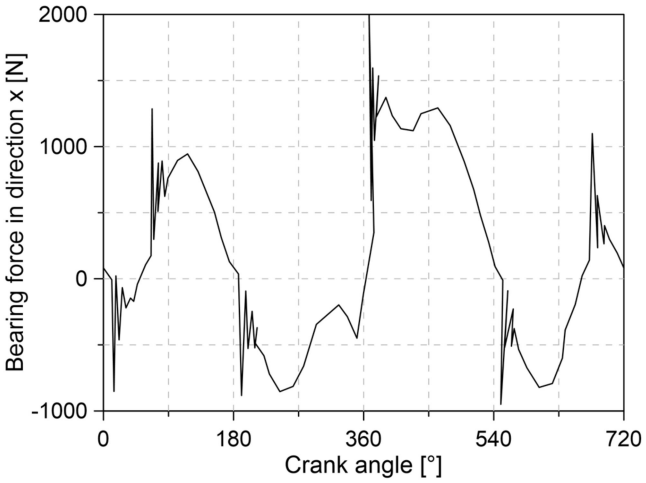

Figure 15. Connecting rod bearing force in the x direction.

It is observed that the force $(F_{cr,x})$ takes positive and negative values in different ranges of crankshaft angle. The change in the direction of the force forces the piston to move to the right or left side of the cylinder liner, causing the lateral movement described in Figure 13a. Additionally, it is observed that the force $(F_{cr,x})$ experiences high fluctuations for the angles 0°, 180°, 360°, 540°, and 720°, which is in agreement with the regions of perturbation of the lateral velocity and the velocity of the inclination angle shown in Figures 13b and 14b. These fluctuations are a consequence of the impact of the piston with the cylinder liner. The above results show the close relationship between the secondary movement of the piston and the force on the connecting rod bearing.

3.3. Piston Slap Force Analysis

Figure 16 shows the slap force for the four endpoints of the piston (see Figure 2) during the combustion cycle.

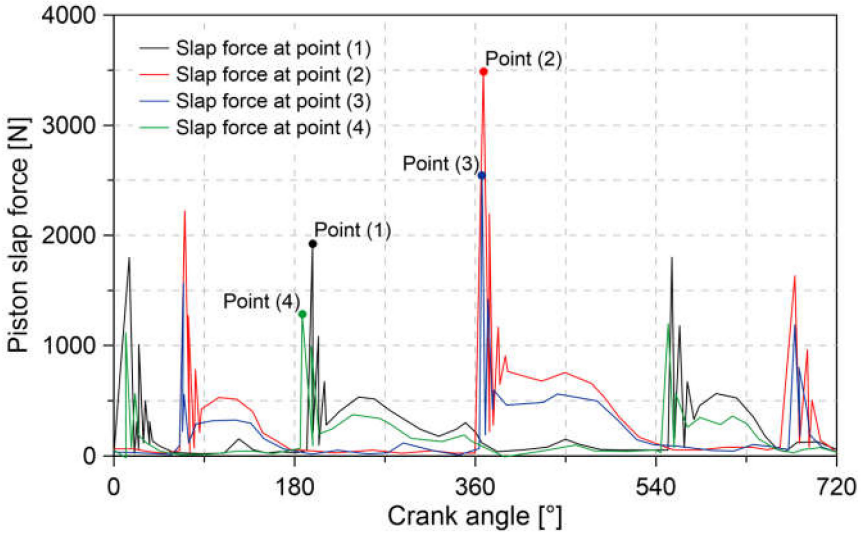

Figure 16. Piston slap force.

It is observed that the impacts on the cylinder liner begin at approximately an angle of 30°, followed by a second sequence of impact located approximately at 45°. The results indicate that the intake and exhaust stages of the engine experience slap forces similarly. The greatest slap force is located at point (2) during the compression stage, which reaches a magnitude of 3480 N. At points (1), (3), and (4), a maximum slap force of 1900 N, 2540 N, and 1275 N, located at 200°, 367°, and 187°, respectively, is observed.

The analysis of the slap force on the piston can be used as a tool for indirect diagnosis of tribological conditions present in the combustion chamber. The increase in slap force is associated with inefficient lubrication between the piston skirt and the cylinder liner. This diagnosis can be made easier since the slap force is associated with engine noise, as indicated in the literature [49].

The conditions of the piston endpoints (1, 2, 3 and 4) can be affected by the position of the piston pin. To study this condition, variations were made in the position of the pin piston through changes in the distance parameter Cp (see Figure 1). The obtained results are shown in Figure 17.

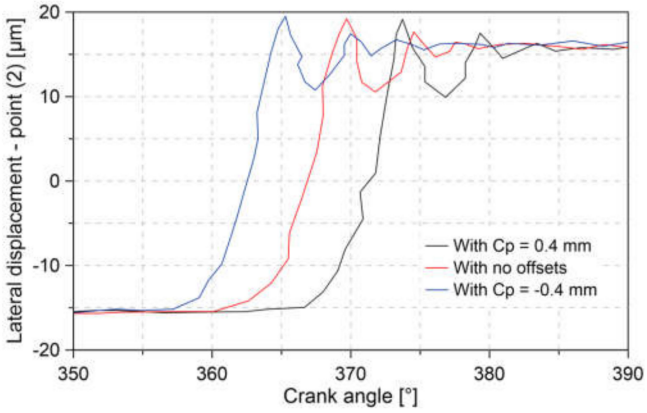

(**a**)

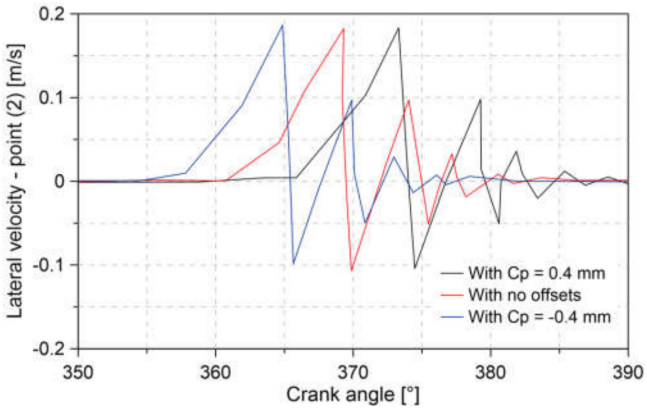

(**b**)

Figure 17. Analysis (**a**) Lateral displacement and (**b**) Lateral velocity for Point (2).

Figure 17 shows the changes in lateral displacement and velocity of point (2) for different values of Cp. The results show that for a positive value of Cp, the piston tends to tilt towards the thrust side, while a negative value causes an inclination towards the anti-thrust side. This difference is located for an angle between 360° and 380°. Similar behavior is observed when evaluating the displacement velocity. In this case, the results indicate a reduction and an increase in velocity for the positive and negative value of Cp.

The change in the movement of point (2) due to the variation of the distance Cp is more noticeable when considering the angle of the inclination of the piston. The changes of this angle are shown in Figure 18.

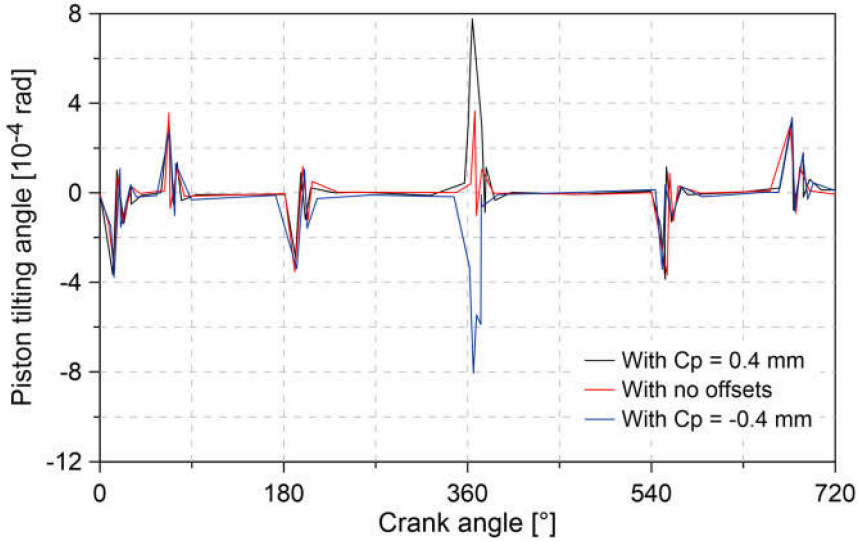

Figure 18. Point (2) tilting angle.

The obtained results show that when using the positive value of Cp, the angle of inclination takes positive values. An opposite case occurs when considering a negative value of Cp. Therefore, the change in the angle of inclination is what causes the piston to move towards the thrust side or anti-thrust side of the cylinder liner.

To analyze the effect of the distance parameter Cp on the slap force, the behavior of the slap force applied at point (2) during the combustion cycle is analyzed. The obtained results are shown in Figure 19.

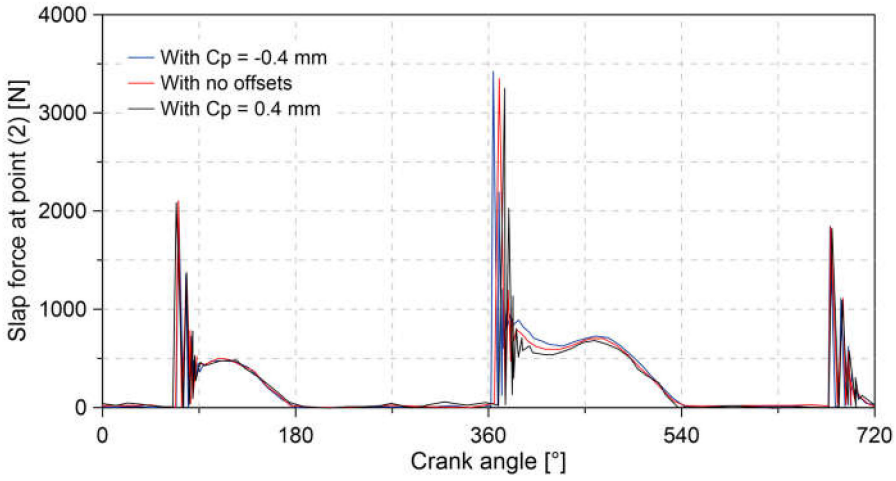

Figure 19. Piston slap force at point (2).

The results of Figure 19 indicate that the magnitude of the force tends to increase if the distance Cp takes a negative value. However, for a positive value of Cp, the slap force is reduced. For the Cp values of −0.4 mm and 0.4 mm, an increase and a reduction of 2% and 3% was observed in the maximum slap force compared to a condition with no offsets (Cp = 0). This behavior is because the change in the direction of the distance Cp causes a reduction or increase in the separation distance between the point (2) and the cylinder liner.

3.4. Effect of Secondary Piston Motion on the Connecting Rod

To analyze the influence of secondary piston movement on the forces of the connecting rod bearings, two different conditions are established in the clearance between the piston skirt and the cylinder liner (Cpc). For this, two values are selected in the Cpc parameter of 0 and 14 µm. The no-clearance condition (Cpc = 0) is used to eliminate the secondary movement of the piston. This is in order to be taken as a reference condition in the analysis.

Figure 20 shows the small end bearing force. The results show that both curves present a similar trend. The difference lies in a series of disturbances throughout the combustion cycle. Each of these disturbances are a consequence of the impact forces on the piston skirt caused by the established clearance (Cpc = 14 um). It is observed that the presence of clearance can cause an increase of 1000 N in the bearing force.

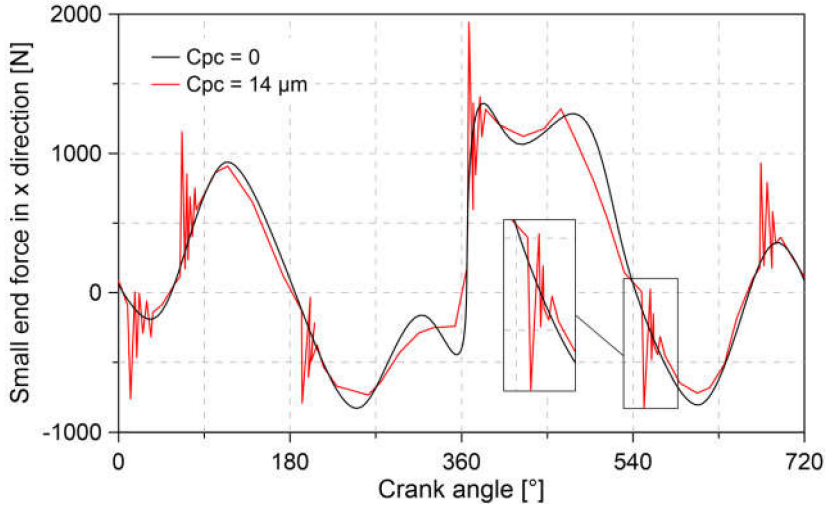

Figure 20. Small end bearing force.

Similarly, Figure 21 shows the big end bearing force. The results show that the presence of the impact forces causes disturbances in the bearing forces. A similar trend to the obtained results in Figure 20 is observed. However, the increase in bearing force is 550 N.

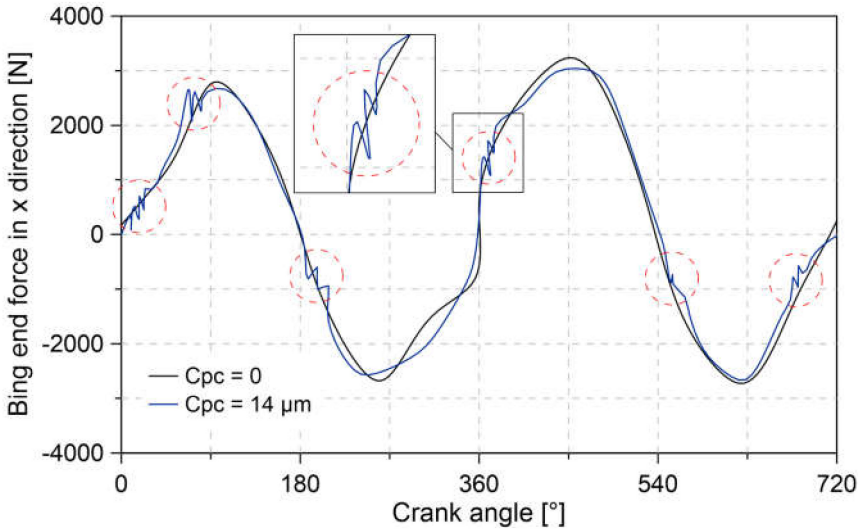

Figure 21. Big end bearing force.

The force disturbances in the connecting rod bearings shown in Figures 20 and 21 are a direct consequence of the contact between the piston skirt and the cylinder liner caused by the clearance Cpc = 14 µm. The main regions of disturbance are located in both cases at a crankshaft angle of 180°, 360°, 540°, and 720°, respectively. This distribution is due to the change in lateral direction experienced by the piston at these locations due to secondary movement, which is in accordance with the results of Figure 13.

3.5. Effect of Clearance on Secondary Piston Motion

Figure 22 depicts the change in lateral displacement and tilt angle for different clearance conditions between the cylinder liner and piston skirt (Cpc).

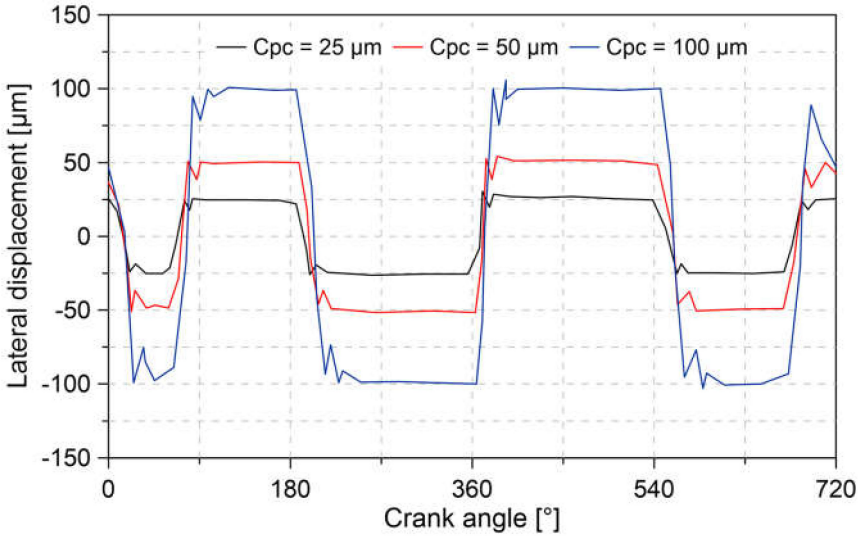

(**a**)

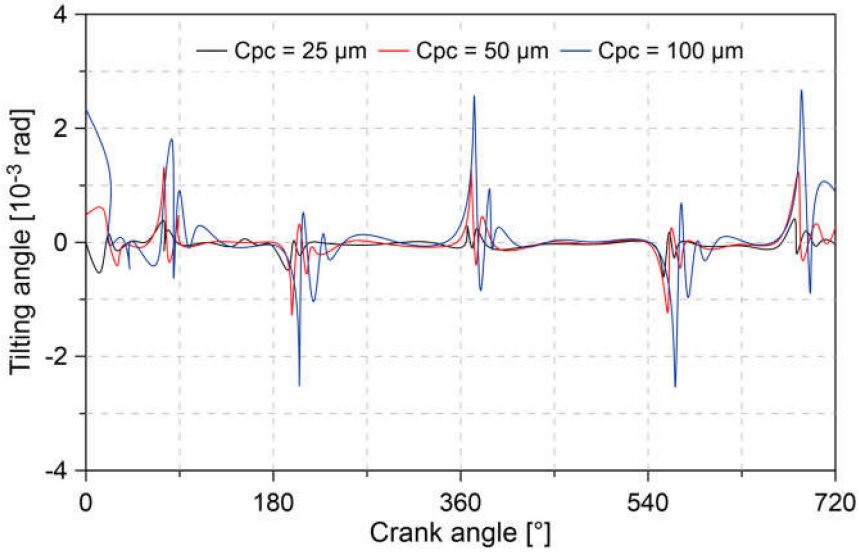

(**b**)

Figure 22. (**a**) Lateral piston motion and (**b**) tilting angle for different Cpc values.

The results show that, for the three values of clearances evaluated, the displacement and angle of inclination curves present similar behavior. However, increasing the clearance Cpc causes an increase in the displacement and an angle of inclination, which is a consequence of the greater travel that the piston must make. The increase in the distance traveled due to the increase in Cpc implies that

the piston has a longer time to reach higher accelerations both in its lateral and angular movement. The increase in acceleration can be verified by observing the behavior of Figure 23.

The results of Figure 23 show that for a distance of 25 µm, 50 µm, and 100 µm in the clearance Cpc, a maximum lateral acceleration of 0.25, 0.58, and 0.86 m/s^2 is obtained, respectively. In the case of angular acceleration, a maximum value of 1.55, 3.02, and 4.87 rad/s^2 was observed.

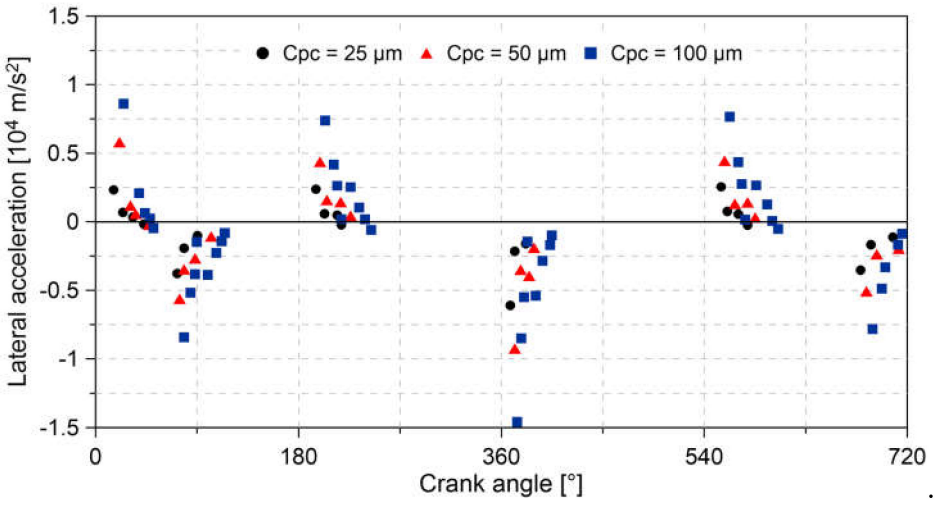

(**a**)

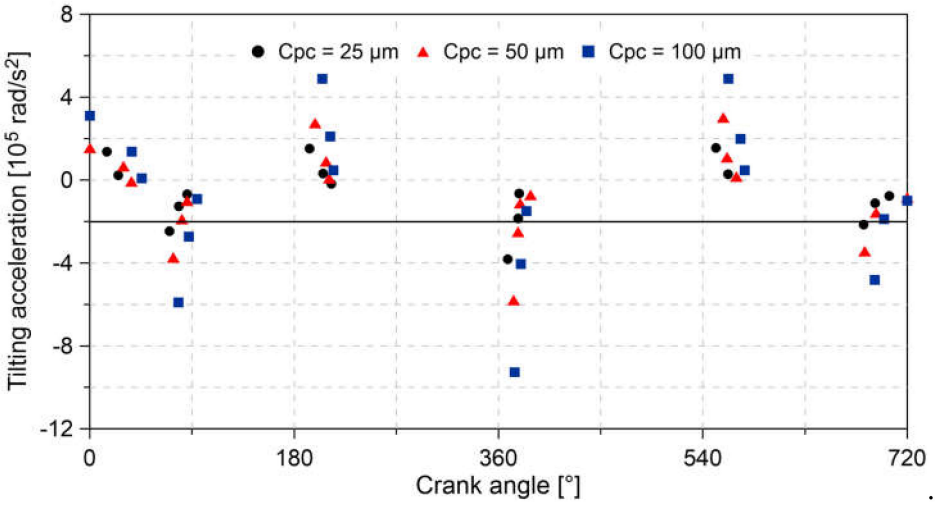

(**b**)

Figure 23. (**a**) Lateral acceleration and (**b**) tilting acceleration at the piston pin.

The effect of increasing clearance Cpc on connecting rod bearing forces can be seen in Figure 24.

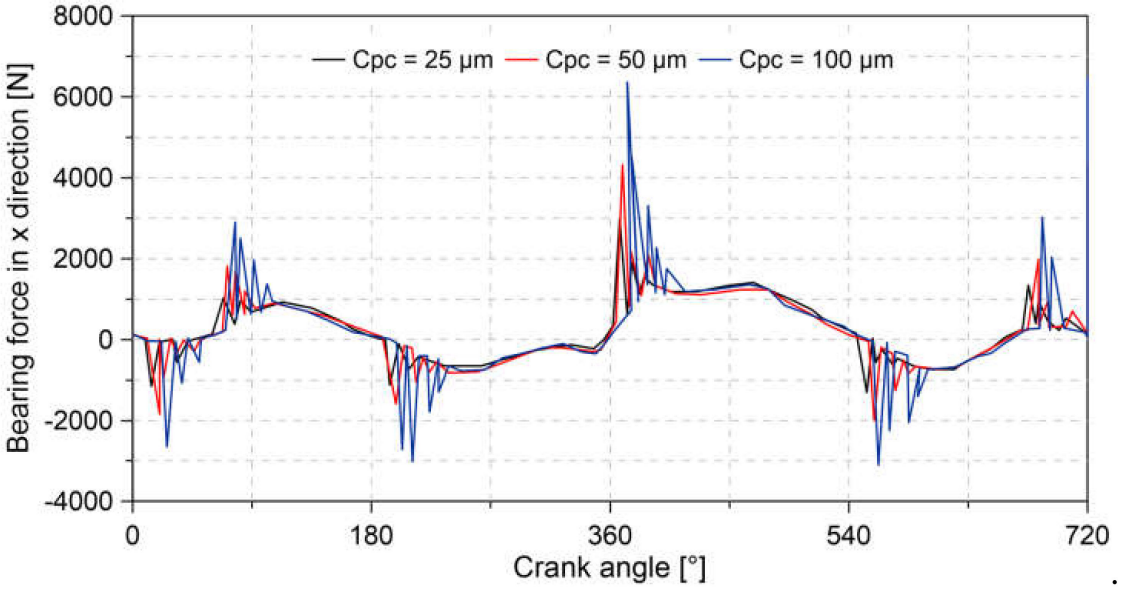

Figure 24. Small end bearing force.

The results show that the higher accelerations in the pin piston due to the increase in the clearance Cpc cause higher impact forces on the connecting rod bearing. A maximum force in the x direction of 2963 N, 4321 N, and 6469 N was observed for a distance of 25 µm, 50 µm, and 100 µm in the Cpc clearance, respectively.

3.6. Effect of Connecting Rod Clearance on Secondary Piston Motion

To evaluate the effect of the connecting rod bearing clearance (Cjb) on the secondary movement of the piston, different values of Cjb were taken in a range of 0–60 µm. For each one of the Cjb values, the acceleration of the lateral motion of the piston was analyzed during a complete cycle. The obtained results are shown in Figure 25.

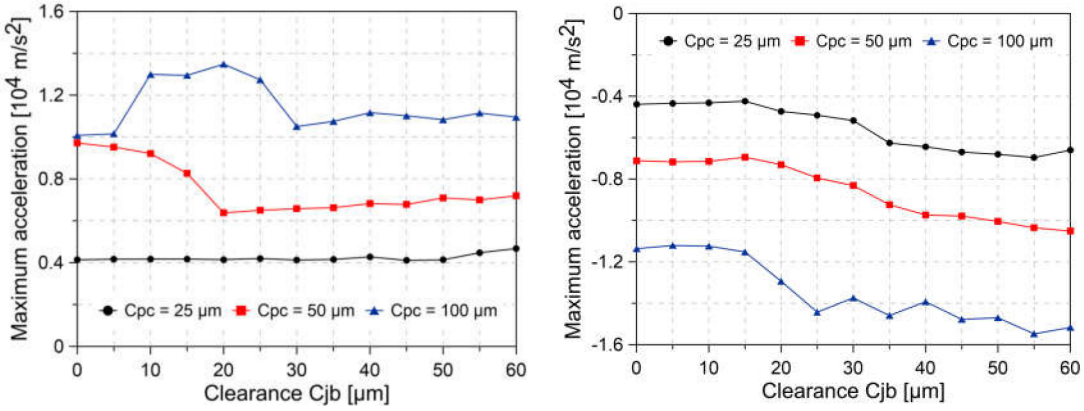

Figure 25. *Cont.*

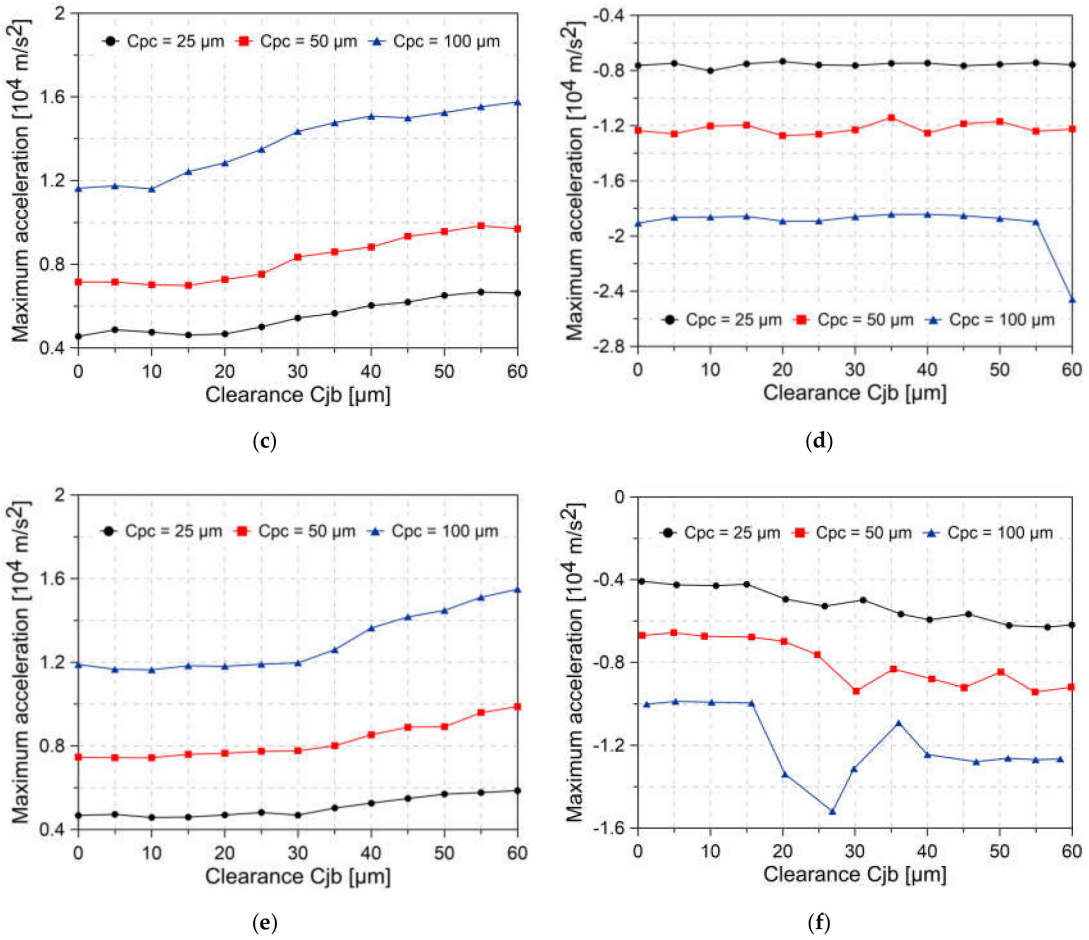

Figure 25. Values of the lateral acceleration of the piston for a crankshaft angle of (**a**) 0–45°, (**b**) 45–90°, (**c**) 180–270°, (**d**) 360–450°, (**e**) 540–630° and (**f**) 630–720°.

It was observed that throughout the combustion cycle, there are different types of trends in lateral acceleration when modifying the Cjb values. In general, a critical value of Cjb is shown, which, when exceeded, produces an increase in lateral acceleration. The behavior described above can be observed for a crankshaft angle of 0–45°. Starting from a slack value of Cjb = 10 µm and Cjb = 25 µm, the magnitude of the acceleration constantly increases for a Cpc value of 25 µm, 50 µm, and 100 µm, respectively. However, for the section of the combustion cycle between 360° and 450°, changes in Cjb do not influence the lateral acceleration of the piston. The above indicates that the impact forces on the piston during the expansion stage are independent of the clearance in the connecting rod bearing (Cjb).

Table 4 shows the limit values of the clearance Cjb for the different ranges of the crankshaft angle and different values for the clearance Cpc.

Table 4. Limit values of Cjb.

Crankshaft Angle (°)	Cpc=25 µm	Cpc=50 µm	Cpc=100 µm
	Clearance Cjb (µm)		
0–45	40.24	19.87	4.82
45–90	14.86	15.16	15.11
180–270	19.92	14.90	9.71
540–630	30.12	25.19	24.89
630–720	15.20	15.07	15.11

The values described in Table 4 indicate the maximum distance that can occur in the clearance Cjb before the lateral acceleration of the piston increases considerably. This could lead to increased impact forces, thus causing vibration and wear problems in the engine. Additionally, the limit values can be used to quantify the wear of the connecting rod bearings and quantify the gravity caused by the secondary movement of the piston.

The analysis of the limit value of Cjb can also be applied considering the primary movement of the piston. Table 5 shows the values of the piston acceleration for different clearance conditions: Cjb and Cpc.

Table 5. Primary piston acceleration (45°–90°).

Clearance Cjb (μm)	**Cpc=25 μm**	**Cpc=50 μm**	**Cpc=100 μm**
	Acceleration (m/s^2)		
0	180	270	300
5	259	299	339
10	198	268	318
15	307	308	408
20	277	417	1147
25	656	1336	1296
30	1015	1855	2335
35	1254	2034	2824
40	1323	2033	3063
45	1382	2332	3132
50	1402	2442	3262
55	1451	2451	3411
60	1530	2490	3410

Table 5 presents a limit value in the clearance Cjb of 25 μm for the range of Cpc values analyzed. A value greater than Cjb = 25 μm causes an increase of approximately 50% in the primary acceleration of the piston.

3.7. Effect of Elastic Deformation of the Piston

The elastic deformation of the piston skirt has an influence on the change of the lubrication thickness (see Equation (21)). This change in thickness caused by the deformation of the piston produces a variation in the piston clearance and, therefore, differences between the estimated slapping forces and, in general, changes in the characteristics of the movement of the piston.

To observe the effect of the elastic deformation of the piston, a comparison is made between the model with deformation and without deformation (d = 0 in Equation (21)). The obtained results are shown in Figure 26.

Figure 26 shows a comparison of the lateral displacement experienced by point (2) (see Figure 3) for the two conditions studied. The results indicate that the model without deformation estimates an increase of 50% in the maximum value of the displacement compared to the elastic model of the piston. This difference could cause an overestimation in the dynamic forces present in the piston-connecting rod–crankshaft system.

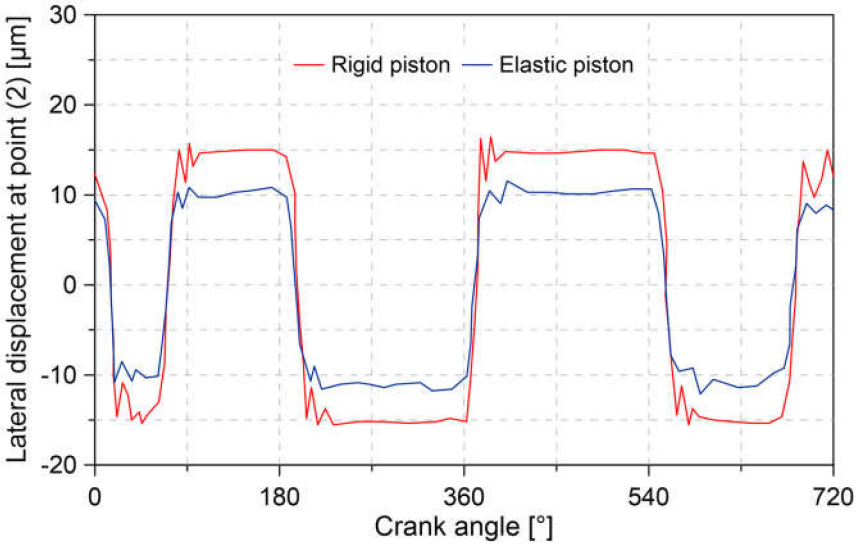

Figure 26. Effect of elastic deformation of the piston.

4. Conclusions

In this study, a mathematical model is carried out in order to analyze the secondary movement of the piston. The model considers deformation due to hydrodynamic pressure and contact pressure in the piston skirt, as well as the influence of clearances in the connecting rod bearings.

The obtained results show that the piston experiences a movement in the lateral direction and an inclination throughout the combustion cycle. In total, six directional changes are recorded in the secondary piston movement with lateral velocities that can reach a maximum of 0.13 m/s. In the case of the angular velocity of the lean angle, the results show maximum velocities close to 4 rad/s. Speed trend analysis indicates that maximum values are reached approximately the top dead center during the compression. The lateral and angular movement of the piston during its travel causes the appearance of impacts on the piston skirt with the cylinder liner. These impacts produce fluctuations in the hydrodynamic forces of the connecting rod bearings in the form of spontaneous increases in force of approximately 500 N.

Analysis of the slap force at the four ends of the piston skirt shows that the range of the maximum magnitudes of the forces is between 1900 N and 3480N. The maximum value of the slap force occurs during the compression stage and is located at the upper ends of the piston skirt. The slap force tends to increase when there are changes in the direction of the parameter Cp. The results indicate that this change in direction can cause a 2% increase in maximum slap force.

The increase in the clearance between the piston skirt and the cylinder liner (Cpc) causes a greater lateral displacement and an increase in the angle of inclination of the piston, which causes an increase in the lateral acceleration of the piston that causes the presence of impact forces of greater magnitude. The results indicate that a 25 µm increase in clearance Cpc can cause the maximum values of the lateral and angular acceleration of the piston to double in value. This increase in acceleration causes a 46% increase in the force of the connecting rod bearings. This behavior shows that the developed model can be used to diagnose the appearance of wear on the cylinder liner. Additionally, the results show that the expansion of the clearance Cpc produces fluctuations in the hydrodynamic force of the big and small bearing of the connecting rod by an average of 775 N.

The analysis of the change in the connecting rod bearing clearance (Cjb) shows that there are critical values in relation to the clearance Cpc, which, when exceeded, produces a constant increase in the lateral acceleration of the piston. This type of trend can also be found by analyzing the primary acceleration of the piston. The results allow us to identify that from a clearance Cjb = 25 µm, there is a drastic increase in the primary acceleration of the piston. The above behavior can be used to diagnose

the conditions of the engine piston, which protects the engine from unwanted vibrations, wear on the connecting rod bearings and wear on the cylinder liner.

Consideration of the elastic deformation of the piston in the model used allows an adequate estimate to be made for the lateral movement of the piston, which affects the dynamic forces in the piston-connecting rod–crankshaft system. It is observed that by not considering the deformation of the piston, there are deviations close to 50% in the lateral displacement of the piston.

Future research on the topic developed aims to improve the instrumentation used for measuring piston clearance. This in order to obtain more accurate results and reduce intrusion on the engine. Additionally, the complexity of the model can be improved, considering other types of deformations, such as those produced by the pressure of the combustion gases at the top of the piston and the thermal deformations of the cylinder bore, which will improve the accuracy in the clearance estimate.

Among the challenges for the application of the methodology used is to guarantee an adequate temperature level in the combustion chamber to avoid damage to the gap sensors. This can be a limitation to evaluate the most critical operating conditions in higher power engines. Additionally, for the comparison between the model estimates and the experimental results, it is necessary to monitor the lubricant temperature since this parameter considerably influences its properties.

Author Contributions: Conceptualization, J.D.F.; methodology, W.P.A., G.V.O., and J.D.F.; software, W.P.A., J.D.F., and G.V.O.; validation, W.P.A., J.D.F., and G.V.O.; formal analysis, W.P.A., J.D.F., and G.V.O.; investigation, W.P.A., J.D.F., and G.V.O.; resources, W.P.A., and J.D.F.; writing—original draft preparation, G.V.O.; writing—review and editing, J.D.F.; funding acquisition, W.P.A., and G.V.O. All authors have read and agreed to the published version of the manuscript.

Funding: This research was supported by the Universidad Francisco de Paula Santander located in Cúcuta, Colombia, the Universidad del Atlántico and Sphere Energy Company located in Barranquilla, Colombia.

Acknowledgments: The authors would like to acknowledge the Universidad del Atlántico, Universidad Francisco de Paula Santander, and Sphere Energy company for their support in the development of this investigation.

Conflicts of Interest: The authors declare no conflict of interest.

Abbreviations

The following abbreviations are used in this manuscript:

Nomenclature

a	Distance between center of gravity of piston body and top of piston skirt
b	Distance between center of piston pin and top of piston skirt
l_1	Separation between the center of gravity of connecting rod and the center of big end bearing
l_2	Separation between the center of gravity of connecting rod and the center of small end bearing
r_p	Piston radius
c_g	Position of center of gravity of piston body offset
g	Gravity
$\ddot{X}_{cr}$	Horizontal acceleration of the center of mass of the connecting rod
$\ddot{Y}_{cr}$	Vertical acceleration of the center of mass of the connecting rod
$F_{TN,h}$	Normal force to hydrodynamic pressure in the film
$F_{TN,c}$	Normal force due to solid to solid contacts
$F_{TF,h}$	Friction force due to hydrodynamic lubricant film
$F_{TF,c}$	Friction force due to solid to solid contacts
$M_{pin,h}$	Moment about the piston pin due to hydrodynamic pressure
$M_{pin,c}$	Moment about the piston pin due to solid to solid contact pressure
$M_{pin,fh}$	Moment about the piston pin due to hydrodynamic friction
$M_{pin,fc}$	Moment about the piston pin due to contact friction
x_{ps}	Lateral displacement of piston skirt
s	Distance between center of piston pin and the contact point
e_d	Radial clearance between the journal–bearing and eccentricity distance
p_r	Pressure of the lubrication film between the journal and the bearing
U_r	Relative tangential velocity between the journal and bearing surface

F	Contact force
H_s	Film thickness ratio
$F_{cr,x}$	Reaction of the piston pin in the x direction
$F_{cr,y}$	Reaction of the piston pin in the y direction
$F_{x,pin}$	Lateral inertia force of piston pin
$F_{y,pin}$	Reciprocating inertia force of piston pin
$F_{x,pis}$	Lateral inertia force of piston
$F_{y,pis}$	Reciprocating inertia force of piston
m_{pis}	Mass of piston
m_{pin}	Mass of piston pin
F_{gases}	Combustion gas force acting on the top of piston
F_{TN}	Side force acting on the piston skirt
F_{TF}	Total friction force acting on the piston skirt
c_p	Position of center of piston pin offset
M_{pin}	Total moment about the piston pin due to all the normal forces
$M_{pin,f}$	Total moment about the piston pin due to all the friction forces
M_{pis}	Inertial moment of piston
L_{ps}	Length of piston skirt
e_b	Eccentricities of piston at the bottom of the skirt
e_t	Eccentricities of piston at the top of the skirt
r	Crankshaft radius of gyration
L_{cr}	Length of connecting rod
F_x	Reaction of bin end in the x direction
F_y	Reaction of bin end in the y direction
m_{rc}	Mass of connecting rod
I_{cr}	Rotary inertia of connecting rod
I_{pis}	Rotary inertia of piston
m_p	Sum of mass of piston and mass of piston pin
h	Oil film thickness
p	Oil film thickness pressure
U	Velocity of piston
C_{pc}	Nominal radial clearance between piston skirt and liner cylinder
d	Elastic deformation of the piston
p_w	Contact pressure distribution
$E\prime$	Composite elastic modulus
$F_{5/2}$	Commutation function
v	Poisson ratio
k_s	Piston stiffness
k_{cs}	Piston contact stiffness
c_d	Piston damping
c_{cd}	Piston contact damping
e_r	Eccentricity ratio of the journal–bearing
C_{jb}	Clearance in the journal–bearing
c_{rc}	Radial clearance
u_f	Coefficient of contact friction
x_b	Displacement of the bearing
x_{cr}	Displacement at the center of gravity of connecting rod

Greek Letters

θ	Crankshaft angle
ϕ	Connecting rod angle
Φ	Pressure flow factors
μ	Dynamic viscosity
σ	Roughness of the surface
φ	Angular coordinate

τ	Shear stress
η	Asperity density
$\overline{\omega}$	Average angular velocity of the journal–bearing
β	Curvature radius
Ψ_f	Term to average the sliding velocity component of the shear stress
Ψ_{fs}	Shear stress factor to consider the effects of surface roughness
Ψ_{fp}	Shear stress factor to consider the waviness
δ_p	Tilting angle of piston skirt
ω	Reference angle of the contact point
ξ	Angular coordinate in bearing model
ζ	Coordinate angle defined by eccentricity vector in bearing model
γ	Angular position of connecting rod

References

1. Han, D.-C.; Lee, J.-S. Analysis of the piston ring lubrication with a new boundary condition. *Tribol. Int.* **1998**, *31*, 753–760. [CrossRef]
2. Amador, G.; Forero, J.D.; Rincon, A.; Fontalvo, A.; Bula, A.; Padilla, R.V.; Orozco, W. Characteristics of Auto-Ignition in Internal Combustion Engines Operated With Gaseous Fuels of Variable Methane Number. *J. Energy Resour. Technol.* **2017**, *139*, 042205. [CrossRef]
3. Consuegra, F.; Bula, A.; Guillín, W.; Sánchez, J.; Duarte Forero, J. Instantaneous in-Cylinder Volume Considering Deformation and Clearance due to Lubricating Film in Reciprocating Internal Combustion Engines. *Energies* **2019**, *12*, 1437. [CrossRef]
4. Duarte Forero, J.; Valencia Ochoa, G.; Piero Rojas, J. Effect of the Geometric Profile of Top Ring on the Tribological Characteristics of a Low-Displacement Diesel Engine. *Lubricants* **2020**, *8*, 83. [CrossRef]
5. Wong, V.W.; Tian, T.; Lang, H.; Ryan, J.P.; Sekiya, Y.; Kobayashi, Y.; Aoyama, S. A Numerical Model of Piston Secondary Motion and Piston Slap in Partially Flooded Elastohydrodynamic Skirt Lubrication. In *Proceedings of the SAE Technical Papers*; SAE: Warrendale, PA, USA, 1994.
6. Valencia Ochoa, G.; Acevedo Peñaloza, C.; Duarte Forero, J. Thermo-economic assessment of a gas microturbine-absorption chiller trigeneration system under different compressor inlet air temperatures. *Energies* **2020**, *12*, 4643. [CrossRef]
7. Ochoa, G.V.; Isaza-Roldan, C.; Duarte Forero, J. Economic and Exergo-Advance Analysis of a Waste Heat Recovery System Based on Regenerative Organic Rankine Cycle under Organic Fluids with Low Global Warming Potential. *Energies* **2020**, *13*, 1317. [CrossRef]
8. Valencia Ochoa, G.; Duarte Forero, J.; Rojas, J.P. A comparative energy and exergy optimization of a supercritical-CO2 Brayton cycle and Organic Rankine Cycle combined system using swarm intelligence algorithms. *Heliyon* **2020**, *6*, e04136. [CrossRef]
9. Ramírez, R.; Gutiérrez, A.S.; Cabello Eras, J.J.; Valencia, K.; Hernández, B.; Duarte Forero, J. Evaluation of the energy recovery potential of thermoelectric generators in diesel engines. *J. Clean. Prod.* **2019**, *241*, 118412. [CrossRef]
10. Valencia Ochoa, G.; Acevedo Peñaloza, C.; Duarte Forero, J. Combustion and Performance Study of Low-Displacement Compression Ignition Engines Operating with Diesel–Biodiesel Blends. *Appl. Sci.* **2020**, *10*, 907. [CrossRef]
11. Kimura, T.; Takahashi, K.; Sugiyama, S. Development of a Piston Secondary Motion Analysis Program with Elastically Deformable Piston Skirt. In *Proceedings of the SAE Technical Papers*; SAE: Warrendale, PA, USA, 1999.
12. Koizumi, T.; Tsujiuchi, N.; Okamura, M.; Kubomoto, I.; Ishida, E. Reduction of piston slap excitation with optimization of piston profile. In *Proceedings of the SAE Technical Papers*; SAE: Warrendale, PA, USA, 2000.
13. Tsujiuchi, N.; Koizumi, T.; Hamada, K.; Okamura, M.; Tsukijima, H. Optimization of Profile fo r Reduction of Piston Slap Excitation. In *Proceedings of the SAE Technical Papers*; SAE: Warrendale, PA, USA, 2004.
14. Murakami, H.; Nakanishi, N.; Ono, N.; Kawano, T. New Three-dimensional Piston Secondary Motion Analysis Method Coupling Structure Analysis and Multi Body Dynamics Analysis. *SAE Int. J. Engines* **2011**, *5*, 42–50. [CrossRef]

15. Diaz, G.A.; Forero, J.D.; Garcia, J.; Rincon, A.; Fontalvo, A.; Bula, A.; Padilla, R.V. Maximum Power From Fluid Flow by Applying the First and Second Laws of Thermodynamics. *J. Energy Resour. Technol.* **2017**, *139*, 032903. [CrossRef]
16. Mejía, A.; Leiva, M.; Rincón-Montenegro, A.; Gonzalez-Quiroga, A.; Duarte-Forero, J. Experimental assessment of emissions maps of a single-cylinder compression ignition engine powered by diesel and palm oil biodiesel-diesel fuel blends. *Case Stud. Therm. Eng.* **2020**, *19*, 100613. [CrossRef]
17. Valencia Ochoa, G.; Cárdenas Gutierrez, J.; Duarte Forero, J. Exergy, Economic, and Life-Cycle Assessment of ORC System for Waste Heat Recovery in a Natural Gas Internal Combustion Engine. *Resources* **2020**, *9*, 2. [CrossRef]
18. Espinel Blanco, E.; Valencia Ochoa, G.; Duarte Forero, J. Thermodynamic, Exergy and Environmental Impact Assessment of S-CO2 Brayton Cycle Coupled with ORC as Bottoming Cycle. *Energies* **2020**, *13*, 2259. [CrossRef]
19. Gutierrez, J.C.; Valencia Ochoa, G.; Duarte-Forero, J. Regenerative Organic Rankine Cycle as Bottoming Cycle of an Industrial Gas Engine: Traditional and Advanced Exergetic Analysis. *Appl. Sci.* **2020**, *10*, 4411. [CrossRef]
20. Dolatabadi, N.; Theodossiades, S.; Rothberg, S.J. Passive Control of Piston Secondary Motion Using Nonlinear Energy Absorbers. *J. Vib. Acoust.* **2017**, *139*. [CrossRef]
21. Lu, Y.; Li, S.; Wang, P.; Liu, C.; Zhang, Y.; Müller, N. The Analysis of Secondary Motion and Lubrication Performance of Piston considering the Piston Skirt Profile. *Shock Vib.* **2018**, *2018*, 3240469. [CrossRef]
22. Tan, Y.-C.; Ripin, Z.M. Analysis of piston secondary motion. *J. Sound Vib.* **2013**, *332*, 5162–5176. [CrossRef]
23. Valencia Ochoa, G.; Piero Rojas, J.; Duarte Forero, J. Advance Exergo-Economic Analysis of a Waste Heat Recovery System Using ORC for a Bottoming Natural Gas Engine. *Energies* **2020**, *13*, 267. [CrossRef]
24. Tan, Y.-C.; Ripin, Z.M. Technique to determine instantaneous piston skirt friction during piston slap. *Tribol. Int.* **2014**, *74*, 145–153. [CrossRef]
25. Meng, F.; Wang, X.; Li, T.; Chen, Y. Influence of cylinder liner vibration on lateral motion and tribological behaviors for piston in internal combustion engine. *Proc. Inst. Mech. Eng. Part J J. Eng. Tribol.* **2015**, *229*, 151–167. [CrossRef]
26. Narayan, S. Effects of Various Parameters on Piston Secondary Motion. In *Proceedings of the SAE Technical Papers*; SAE: Warrendale, PA, USA, 2015.
27. Obert, P.; Müller, T.; Füßer, H.-J.; Bartel, D. The influence of oil supply and cylinder liner temperature on friction, wear and scuffing behavior of piston ring cylinder liner contacts—A new model test. *Tribol. Int.* **2016**, *94*, 306–314. [CrossRef]
28. Mazouzi, R.; Kellaci, A.; Karas, A. Effects of piston design parameters on skirt-liner dynamic behavior. *Ind. Lubr. Tribol.* **2016**, *68*, 250–258. [CrossRef]
29. Fang, C.; Meng, X.; Xie, Y. A piston tribodynamic model with deterministic consideration of skirt surface grooves. *Tribol. Int.* **2017**, *110*, 232–251. [CrossRef]
30. Meng, F.M.; Zhang, Y.Y.; Hu, Y.Z.; Wang, H. Thermo-elasto-hydrodynamic lubrication analysis of piston skirt considering oil film inertia effect. *Tribol. Int.* **2007**, *40*, 1089–1099. [CrossRef]
31. Zhang, Z.; Xie, Y.; Zhang, X.; Meng, X. Analysis of piston secondary motion considering the variation in the system inertia. *Proc. Inst. Mech. Eng. Part D J. Automob. Eng.* **2009**, *223*, 549–563. [CrossRef]
32. Meng, X.; Xie, Y. A new numerical analysis for piston skirt–liner system lubrication considering the effects of connecting rod inertia. *Tribol. Int.* **2012**, *47*, 235–243. [CrossRef]
33. Meng, X.; Ning, L.; Xie, Y.; Wong, V.W. Effects of the connecting-rod-related design parameters on the piston dynamics and the skirt–liner lubrication. *Proc. Inst. Mech. Eng. Part D J. Automob. Eng.* **2013**, *227*, 885–898. [CrossRef]
34. Zhu, J.; Zhu, H.; Fan, S.; Xue, L.; Li, Y. A study on the influence of oil film lubrication to the strength of engine connecting rod components. *Eng. Fail. Anal.* **2016**, *63*, 94–105. [CrossRef]
35. Pelosi, M.; Ivantysynova, M. Heat transfer and thermal elastic deformation analysis on the piston/cylinder interface of axial piston machines. *J. Tribol.* **2012**, *134*, 041101. [CrossRef]
36. Ning, L.; Meng, X.; Xie, Y. Incorporation of deformation in a lubrication analysis for automotive piston skirt–liner system. *Proc. Inst. Mech. Eng. Part J J. Eng. Tribol.* **2013**, *227*, 654–670. [CrossRef]
37. Flores, P. A parametric study on the dynamic response of planar multibody systems with multiple clearance joints. *Nonlinear Dyn.* **2010**, *61*, 633–653. [CrossRef]

38. Daniel, G.B.; Cavalca, K.L. Analysis of the dynamics of a slider–crank mechanism with hydrodynamic lubrication in the connecting rod–slider joint clearance. *Mech. Mach. Theory* **2011**, *46*, 1434–1452. [CrossRef]
39. Flores, P.; Ambrósio, J.; Claro, J.C.P.; Lankarani, H.M. Influence of the contact—Impact force model on the dynamic response of multi-body systems. *Proc. Inst. Mech. Eng. Part K J. Multi-Body Dyn.* **2006**, *220*, 21–34. [CrossRef]
40. Daniel, G.B.; Machado, T.H.; Cavalca, K.L. Investigation on the influence of the cavitation boundaries on the dynamic behavior of planar mechanical systems with hydrodynamic bearings. *Mech. Mach. Theory* **2016**, *99*, 19–36. [CrossRef]
41. Patir, N.; Cheng, H.S. Application of Average Flow Model to Lubrication Between Rough Sliding Surfaces. *J. Lubr. Technol.* **1979**, *101*, 220–229. [CrossRef]
42. Patir, N.; Cheng, H.S. An Average Flow Model for Determining Effects of Three-Dimensional Roughness on Partial Hydrodynamic Lubrication. *J. Lubr. Technol.* **1978**, *100*, 12–17. [CrossRef]
43. Greenwood, J.A.; Tripp, J.H. The contact of two nominally flat rough surfaces. *Proc. Inst. Mech. Eng.* **1970**, *185*, 625–633. [CrossRef]
44. Hays, D.F. Theory of hydrodynamic lubrication. *J. Frankl. Inst.* **1961**, *272*, 521–522. [CrossRef]
45. DuBois, G.B.; Ocvirk, F.W. *Analytical Derivation and Experimental Evaluation of Short-Bearing Approximation for Full Journal Bearings*; National Advisory Committee for Aeronautics: Kitty Hawk, NC, USA, 1953.
46. Zhu, D.; Hu, Y.-Z.; Cheng, H.S.; Arai, T.; Hamai, K. A Numerical Analysis for Piston Skirts in Mixed Lubrication: Part II—Deformation Considerations. *J. Tribol.* **1993**, *115*, 125–133. [CrossRef]
47. Cantore, G.; Giacopini, M.; Rosi, R.; Strozzi, A.; Pelloni, P.; Forte, C.; Achiluzzi, M.; Bianchi, G.M.; Ceschini, L.; Morri, A. Validation of a combined CFD/FEM methodology for the evaluation of thermal load acting on aluminum alloy pistons through hardness measurements in internal combustion engines. *Metall. Sci. Tecnol.* **2011**, *29*, 16–25.
48. McFadden, P.D.; Turnbull, S.R. Dynamic analysis of piston secondary motion in an internal combustion engine under non-lubricated and fully flooded lubricated conditions. *Proc. Inst. Mech. Eng. Part C J. Mech. Eng. Sci.* **2011**, *225*, 2575–2585. [CrossRef]
49. Zavos, A.; Nikolakopoulos, P.G. Measurement of friction and noise from piston assembly of a single-cylinder motorbike engine at realistic speeds. *Proc. Inst. Mech. Eng. Part D J. Automob. Eng.* **2018**, *232*, 1715–1735. [CrossRef]